

Mars' External Magnetic Field as Seen from the Surface with InSight

Anna Magdalena Mittelholz¹, Catherine L. Johnson², Matthew O. Fillingim³, Robert E. Grimm⁴, Steven Peter Joy⁵, Shea N. Thorne⁶, and William Bruce Banerdt⁷

¹Harvard University

²University of British Columbia

³University of California, Berkeley

⁴Southwest Research Institute

⁵University of California Los Angeles

⁶The University of British Columbia

⁷Jet Propulsion Laboratory

February 22, 2024

Abstract

The magnetometer of the InSight mission operated on the martian surface from November 2018 until May 2022. Previously, satellites have provided information on the martian magnetic field environment from orbit, however, the degree to which external fields penetrate to and interact with the surface could not be studied prior to the InSight landing. Here, we present an overview of the complete surface magnetic field data from InSight sols 14 to 1241 that display different external magnetic field phenomena, transient and periodic. Periodic observations range from short period waves (100s-1000s of seconds), diurnal variations, ~26 sol Carrington rotations, to seasonal fluctuations. Transient events are observed in response to space weather and dust movement. We find that ionospheric variations are the dominant contribution as seen from the surface, while contributions from the undisturbed IMF are more subtle. We discuss limitations associated with a single point measurement and opportunities that future missions could enable. Including magnetometers on future missions at a variety of locations for long-duration continuous observations will be of great value in understanding a range of external field phenomena and will enable further investigations in different crustal magnetic field settings.

Mars' External Magnetic Field as Seen from the Surface with InSight

A. Mittelholz¹, C. L. Johnson^{2,3}, M. Fillingim⁴, R. E. Grimm⁵, S. Joy⁶, S. N.
Thorne², W. B. Banerdt⁷

¹Department of Earth and Planetary Sciences, Harvard University, Cambridge, MA, USA.

²Department of Earth, Ocean and Atmospheric Sciences, The University of British Columbia, Vancouver,
Canada.

³Planetary Science Institute, Tucson, Arizona, USA.

⁴Space Sciences Laboratory, University of California, Berkeley, USA.

⁵Southwest Research Institute, Boulder, USA.

⁶Department of Earth, Planetary, and Space Sciences, University of California, Los Angeles, USA.

⁷Jet Propulsion Laboratory, California Institute of Technology, Pasadena, USA.

Key Points:

- InSight's magnetometer provides the first surface recordings of the martian magnetic field environment over 1241 sols.
- Transient and periodic external fields with time scales of minutes up to a year are observed and their origins discussed.
- Time variations in the surface magnetic field are primarily driven by the ionosphere, affected by atmospheric seasonal variations.

Corresponding author: Anna Mittelholz, amittelholz@fas.harvard.edu

Abstract

20 The magnetometer of the InSight mission operated on the martian surface from Novem-
21 ber 2018 until May 2022. Previously, satellites have provided information on the mar-
22 tian magnetic field environment from orbit, however, the degree to which external fields
23 penetrate to and interact with the surface could not be studied prior to the InSight land-
24 ing. Here, we present an overview of the complete surface magnetic field data from In-
25 Sight sols 14 to 1241 that display different external magnetic field phenomena, transient
26 and periodic. Periodic observations range from short period waves (100s-1000s of sec-
27 onds), diurnal variations, ~ 26 sol Carrington rotations, to seasonal fluctuations. Tran-
28 sient events are observed in response to space weather and dust movement. We find that
29 ionospheric variations are the dominant contribution as seen from the surface, while con-
30 tributions from the undisturbed IMF are more subtle. We discuss limitations associated
31 with a single point measurement and opportunities that future missions could enable.
32 Including magnetometers on future missions at a variety of locations for long-duration
33 continuous observations will be of great value in understanding a range of external field
34 phenomena and will enable further investigations in different crustal magnetic field set-
35 tings.
36

Plain Language Summary

37
38 The magnetometer of the InSight mission has measured the magnetic field at the
39 planetary surface for the first time. Although satellites previously sampled the magnetic
40 field globally from orbit, InSight enables a local view from the surface. Here we focus
41 on time-varying magnetic fields driven by the Sun and the uppermost region of the at-
42 mosphere (the ionosphere); this includes the interplanetary magnetic field (IMF) and the
43 ionosphere interacting with the planet. A range of physical phenomena can be observed.
44 Some of those are periodic, such as the diurnal signature or seasonal variations, some
45 are transient, such as the effect of space weather. We find that ionospheric variations are
46 the dominant signal at the surface. We discuss limitations of such observations due to
47 the single point measurement and possibilities future missions will provide.

48 1 Introduction

49 InSight, Interior Exploration using Seismic Investigations, Geodesy and Heat Trans-
 50 port, landed on Mars in Elysium Planitia at 4.5°N and 135.6°W in November 2018. The
 51 mission’s primary goal is to study the interior of Mars (Banerdt et al., 2020), using ob-
 52 servations made by the main science instruments: a seismometer, a heatflow probe and
 53 radio antennas. The InSight Fluxgate (IFG) magnetometer is part of the Auxiliary Pay-
 54 load Sensor System (APSS; (Banfield et al., 2018)), that was included to characterize
 55 environmental conditions around the lander to which the seismometer is sensitive. As
 56 such, the IFG is not a primary science instrument; it is however the first surface mag-
 57 netometer on Mars’ surface and has been providing unprecedented scientific information
 58 on the martian magnetic field environment (Johnson et al., 2020).

59 The IFG measures the vector magnetic field, that comprises contributions from in-
 60 ternal and external magnetic fields, as well as from the lander itself. The latter are es-
 61 timated and subtracted from the data as part of the calibration process that has been
 62 discussed elsewhere (Joy et al., 2019; Mittelholz, Johnson, Thorne, et al., 2020; Russell
 63 & Joy, 2020). Internal fields are generated below the planetary surface and result from
 64 remanent crustal magnetization acquired in an ancient field, initially detected from or-
 65 bit by the Mars Global Surveyor (MGS) spacecraft (Acuna et al., 1999). External mag-
 66 netic fields are generated by sources above the planetary surface, such as the ionosphere
 67 or the interplanetary magnetic field (IMF). InSight’s findings related to the crustal mag-
 68 netic field have been detailed previously (Johnson et al., 2020). We provide a brief sum-
 69 mary here as context for the environment in which external fields are measured, and fo-
 70 cus on the latter in this paper.

71 The InSight landing site is in a region of moderately-strong magnetized crust com-
 72 pared with other regions on Mars as seen from orbit (Smrekar et al., 2018; Langlais et
 73 al., 2019; Mittelholz et al., 2018). IFG data have shown that the surface magnetic field
 74 intensity is about 2000 nT, ~ 10 times stronger than predicted from orbital measurements.
 75 This indicates the presence of magnetization at spatial scales smaller than ~ 150 km (Johnson
 76 et al., 2020), the lowest orbital altitudes of satellite measurements from the Mars Atmo-
 77 sphere and Volatile Evolution (MAVEN) mission (Jakosky et al., 2015). The minimum
 78 magnetization required to explain magnetic field observations is consistent with an an-
 79 cient dynamo field with Earth-like strength (Johnson et al., 2020) and could support an
 80 early (~ 4 Ga) (Acuna et al., 1999; Lillis et al., 2013; Vervelidou et al., 2017), a late (Schubert
 81 et al., 2000) or a continuous or interrupted, long-lived dynamo (Mittelholz, Johnson, Fein-
 82 berg, et al., 2020), depending on the buried unit(s) that carry the magnetization (Johnson
 83 et al., 2020; Knapmeyer-Endrun et al., 2021; Wiczorek et al., 2022).

84 External time varying magnetic fields comprise the rest of the naturally-occurring
 85 signal, and result from time-dependent processes in the overall Martian magnetic envi-
 86 ronment (Figure 1). The solar wind in which the IMF is embedded is decelerated from
 87 supersonic to subsonic velocities at the bow shock due to the martian obstacle. IMF field
 88 lines drape around the planet, and are compressed below the bowshock (Nagy et al., 2004).
 89 The magnetic pileup boundary (MPB) separates the upper magnetosheath (MS), a re-
 90 gion with strong wave activity, from the lower magnetic pileup region. Solar photons (UV
 91 and X-rays) and energetic particles in the solar wind ionize the neutral atmosphere es-
 92 pecially on the day-side to build up the ionosphere. Ionospheric pressure and crustal mag-
 93 netic fields help to stand off the solar wind from the surface.

94 As a result of this magnetic field environment, periodic and transient magnetic fields
 95 driven by different mechanisms can be expected (Table 1). Those mechanisms are re-
 96 lated to the IMF and the solar wind itself, or the ionized part of the planetary atmosphere,
 97 the ionosphere. The planet’s rotation in the solar wind leads to diurnal fluctuations, and
 98 enhanced fields during the day-time. The annual cycle is driven by Mars’ eccentric or-
 99 bit around the Sun and associated change in dynamic pressure, and the tilt of its rota-

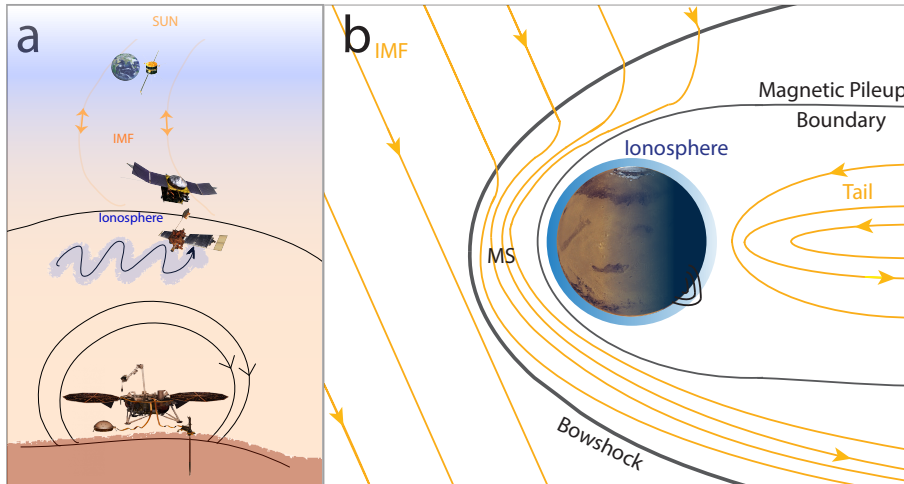


Figure 1. (a) Cartoon of the magnetic field environment as seen from InSight (b) An overview of the magnetic field environment of Mars. MS=Magnetosheath. (a)+(b) Not to scale.

100 tion axis resulting in more or less favourable crustal field interaction due to the concen-
 101 tration of the crustal fields in the Southern hemisphere. The rotation of the Sun results
 102 in a change in the position of Mars with respect to the heliospheric current sheet (i.e.,
 103 above or below), and thus a polarity change of the interplanetary magnetic field at Mars
 104 every ~ 13 days. At shorter periods, around 100-1000 seconds, interaction of the solar
 105 wind with the martian magnetosphere can lead to ultra low frequency (ULF) waves. Tran-
 106 sient fields associated with solar activity, i.e. space weather, impinge on and interact with
 107 Mars' magnetosphere. Another source of time-varying fields is the ionosphere. Changes
 108 in the neutral atmosphere and/or electron density lead to diurnal, and also seasonal changes.
 109 The Sun-facing or day-side of the planet is ionized by solar photons and energetic par-
 110 ticles, and recombination of charged particles largely neutralize this effect at the night-
 111 side, leading to diurnal magnetic field variations. Neutral winds in the atmosphere vary
 112 with season and affect currents produced in the ionospheric dynamo region. Addition-
 113 ally, aperiodic variations result from dust storms, that in turn have a seasonal occurrence.
 114 Dust absorbs solar radiation leading to thermal expansion of the atmosphere, raising the
 115 altitude of the entire atmospheric column including the ionosphere (Withers & Pratt,
 116 2013), and can thus have an effect on magnetic fields at the ground resulting from iono-
 117 spheric currents. In addition, local surficial dust movement can lead to triboelectric ef-
 118 fects; the charged dust grains in suspension generate small amplitude, transient magnetic
 119 fields that are not directly related to the IMF or the ionosphere.

120 In the following, we focus on time varying magnetic fields as seen from the surface.
 121 To give context for these new observations we provide a short overview of satellite ob-
 122 servations of external fields (Section 2). In Section 3 we introduce the data sets used in
 123 this paper. We show InSight IFG data collected throughout the entire mission time frame
 124 (up to sol 1241), but mainly focus on data from the first 736 sols, which provide a mostly
 125 continuous data set. In section 4, we describe surface magnetic field observations struc-
 126 tured by period. In that section we summarize previous findings, and report new results
 127 enabled by the full time series. Lastly, we discuss the implications of observations for mag-
 128 netic sounding of the planetary interior (Section 5.1) and summarize some of the open
 129 questions to motivate magnetometers on future missions to Mars (Section 5.2).

Table 1. External magnetic fields with InSight

Periodicity	Cause	Detection	Literature
Seasonal	Ionospheric Fluctuations; secondary: Heliospheric Distance	Yes	Mittelholz, Johnson, Thorne, et al. (2020, 2021)
Carrington Rotation	IMF	Yes	A Mittelholz et al. (2022); Luo et al. (2022)
Daily + harmonics	Ionospheric Fluctuations	Yes	Mittelholz, Johnson, Thorne, et al. (2020); Johnson et al. (2020); Luo et al. (2022)
Short - period	Interaction of Solar Wind with Mars	Yes	Chi et al. (2019); Johnson et al. (2020)
Transient: Space Weather	Transients in the Solar Wind	Yes	Mittelholz, Johnson, Fillingim, et al. (2021)
Transient: Dust Movement	Dust movement	likely, but rare	Charalambous et al. (2021); Thorne et al. (2022)

2 Brief Summary of Satellite Observations

Two satellite missions have provided magnetic field data sets at Mars (Mittelholz & Johnson, 2022): MGS (Acuna et al., 1999) and MAVEN (Jakosky et al., 2015). MGS (1997-2006) data were acquired mainly in a 400 km altitude, 2 am – 2 pm orbit around Mars. In contrast, the MAVEN orbit (2014-present) covers a variety of altitudes from approximately 135 km altitude up to above the bow shock at varying local times (Mittelholz et al., 2018). The wealth of satellite data mapping the magnetic field and plasma environment around Mars has enabled a wide range of external field studies from orbit (e.g., (Brain et al., 2003, 2006; Fillingim et al., 2010, 2012; Mittelholz et al., 2017; Ramstad et al., 2020)). We give a short summary of some key satellite-derived magnetic field observations, starting with space weather and then organized by periodicity.

Space Weather: Space weather is a generic term for transient changes in solar wind conditions and the resulting effects on interactions with planets/moons. A corotating interaction region (CIR) occurs when high speed solar wind streams originating from coronal holes overtake slower solar wind forming a region of compressed plasma. A coronal mass ejection (CME) is a large expulsion of plasma and magnetic field from the solar corona, and is referred to as an interplanetary CME (ICME) as it travels through the solar system. Depending on their propagation speed relative to the ambient solar wind speed, ICMEs can produce a shock wave in the solar wind. The velocity, density, and temperature of solar wind plasma can exhibit sharp changes at the leading edge of the ICME, followed by the strongly magnetized coronal ejecta in the ICME core, that may extend the interaction of the ICME with Mars for up to several days.

Orbital magnetic field observations of space weather at Mars come from MGS (Crider et al., 2003; Xu et al., 2019; Espley et al., 2005) and MAVEN (Jakosky et al., 2015; Luhmann et al., 2017; Lee et al., 2017, 2018; Xu et al., 2019). MAVEN’s mission goal includes characterization of space weather and MAVEN’s eccentric orbit which traverses the mar-

156 tian magnetosphere and the solar wind, in combination with the spacecraft instrument
 157 suite, is particularly suited for space weather observations. Magnetic observations are
 158 preferentially made in the IMF where the effects of space weather can usually be seen
 159 as a sudden enhancement in the field (e.g., (Jakosky et al., 2015; Lee et al., 2017, 2018)).
 160 Within the magnetosheath or pile-up region, the signature of space weather is compli-
 161 cated by the ionospheric response, which in turn is highly variable and dependent on lo-
 162 cal ionospheric conditions and on the complex interactions of ionospheric currents with
 163 crustal fields and the IMF. For a review of space weather observations at Mars during
 164 solar cycle 23 we refer to (Lee et al., 2017).

165 *Annual:* Magnetic field signals with annual periodicities have been observed in
 166 satellite data, but are limited by mission durations. MGS data show that peak magnetic
 167 field amplitudes tend to occur near perihelion, when Mars is closest to the Sun (Mittelholz
 168 et al., 2017). The magnetic field amplitude falls off with heliocentric distance, i.e., as $1/r$,
 169 consistent with fluid solar wind model predictions, in which the decrease in solar wind
 170 pressure with distance from the Sun is balanced by a decreased magnetic pressure (pro-
 171 portional to $|B|^2$). The sunward component of the IMF is larger for a planet closer to
 172 the sun, where the IMF is more radial, and decreases with increasing heliocentric dis-
 173 tance and Parker spiral angle (Figure 1a). Seasonal variability in the neutral atmosphere
 174 also leads to associated effects in the ionosphere (Lillis et al., 2019; Mittelholz, Johnson,
 175 Thorne, et al., 2020) and can alter ionospheric peak altitudes by ± 10 km (Morgan et al.,
 176 2008; Felici et al., 2020). During seasonally occurring dust storms, thermal expansion
 177 of the atmospheric column raises the altitude of any given isobar; because peak electron
 178 densities in the Mars ionosphere occur at a pressure of ~ 1 nPa times the cosine of the
 179 solar zenith angle (Withers, 2009) this leads to an increase in ionospheric peak altitude
 180 for regional and large dust storms respectively (Withers & Pratt, 2013).

181 *Solar Rotation:* The solar rotation period as seen from Mars of about 26.3 days
 182 (Carrington rotation) is seen in orbital magnetic field observations as fluctuations in field
 183 strength of about 10 nT at 400 km (Brain et al., 2006; Mittelholz et al., 2017; Ferguson
 184 et al., 2005), and a polarity change in the magnetic field. At ~ 400 km altitude the IMF
 185 can be described as a draped field and so the horizontal components dominate.

186 *Diurnal:* Diurnal periodicity in MGS data has been quantified and modeled (Mittelholz
 187 et al., 2017; Olsen et al., 2010; Ferguson et al., 2005). The difference in the average large
 188 scale structure (i.e., up to spherical harmonic degree 5 in global models) at 400 km al-
 189 titude between the day side and the night-side ranges from -30 nT to 30 nT, but con-
 190 siderably larger fluctuations can occur on a day-to-day basis (Mittelholz et al., 2017).

191 *Short Period Waves:* Short period waves, often referred to as pulsations or ULF
 192 waves, have been attributed to compressional oscillations in the magnetotail and Kelvin-
 193 Helmholtz instabilities. These typically exhibit power in the horizontal components and
 194 range from mHz to Hz. Observations of ULF waves at Mars were made by the Phobos-
 195 2 spacecraft (Sagdeev & Zakharov, 1989) and later by other spacecraft such as MGS (Brain
 196 et al., 2002; Espley et al., 2004). Studies of the lowest segments of MGS orbits allowed
 197 identification of ULF waves at ionospheric altitudes (Espley et al., 2006). MAVEN data
 198 (Connerney et al., 2015; Harada et al., 2019) have allowed investigations of newly-identified
 199 compressional narrow band emissions in the day-side upper ionosphere and in the night-
 200 side magnetotail (Harada et al., 2019). We refer to Glassmeier and Espley (2013) for a
 201 more complete (but pre-MAVEN) review of ULF waves.

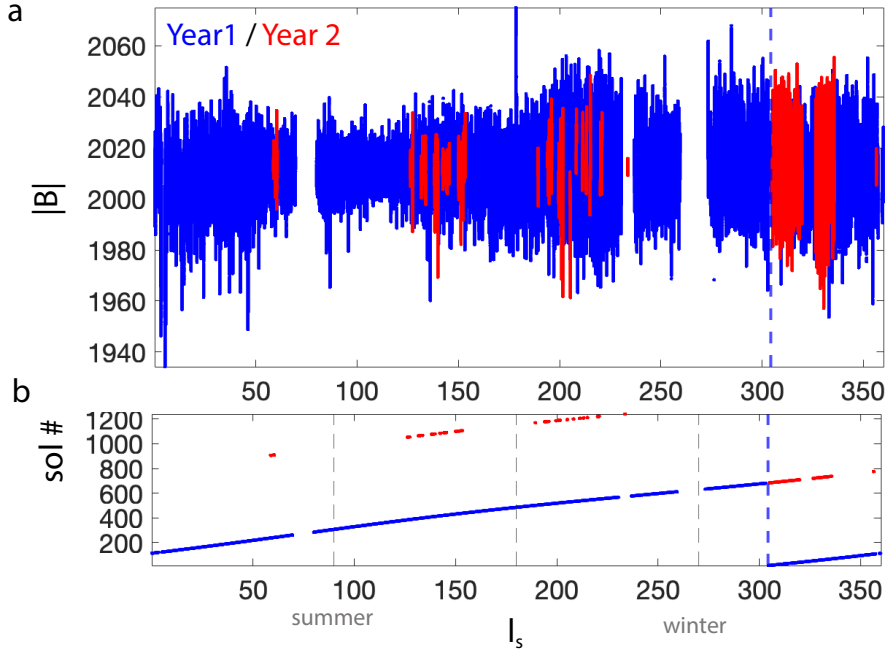


Figure 2. Magnetic field amplitude, $|B|$, measured at the InSight landing site versus solar longitude (l_s) during Martian years 1 (blue) and 2 (red) of IFG operations. All data up to sol 1241 of InSight operations are included. The blue vertical dashed line marks the beginning of the mission. (b) Corresponding InSight mission sol numbers. Vertical dashed lines indicate solstices and equinoxes.

3 Data Sets

3.1 InSight Fluxgate Magnetometer

InSight’s magnetometer has been collecting data since sol 14 of the mission (Figure 2). The magnetometer operated (almost) continuously from December 11, 2018 to January 31, 2021, i.e., sols 14-736, spanning over one martian year (Figure 3). Gaps in the continuous data are mostly related to intermittent outages of the APSS data acquisition electronics and/or communication issues during solar conjunction. Subsequent, intermittent data collection resulted from power constraints due to dust accumulation on the solar panels. These later data typically span only partial sols and the last ~ 5 hours of data were acquired on sol 1241, on May 24, 2022. In Mars year one, 90% of all 610 sols for which data were acquired cover the full day, in year two data were acquired on 102 sols, but the IFG was operating for the full day for only 38% of those sols, and no further IFG data are currently anticipated.

We use the publicly-available, calibrated IFG data at 0.2 Hz sampling (V6 in the Planetary Data System; Russell and Joy (2020)). For intervals for which the IFG sampled at 2 Hz (sol 189 onwards), we use data down-sampled to 0.2 Hz on the ground (labelled as gpt2 on the PDS). The data is in lander level frame (Joy et al., 2019), a local frame in which the field components B_N , B_E and B_D are North, East and Down.

3.2 Satellite Magnetometer Data

MAVEN data are used for comparison with InSight observations at longer periods, specifically solar rotations. Although MAVEN measurements are available throughout

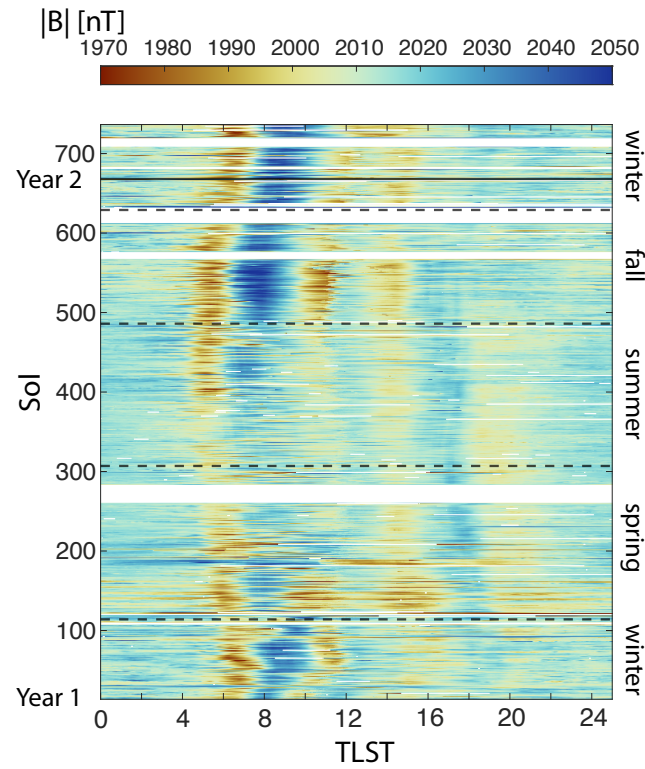


Figure 3. The magnetic field amplitude, $|B|$, versus true local solar time (TLST) for sols 14-736, the time of continuous IFG operations. Data are binned in 30-second bins and the mean for each bin is shown. Dashed lines indicate solstices and equinoxes. The solid line marks sol 668 and the start of InSight's second year on Mars.

223 the InSight mission, the precessing orbit means that they are only occasionally acquired
 224 directly overhead the InSight landing site. Furthermore, the changing orbit geometry,
 225 means that MAVEN orbits over the InSight landing site are at differing altitudes and
 226 local times. Thus a direct comparison of individual orbital tracks with IFG data is not
 227 our focus here, but has been the subject of separate studies (Fillingim et al., 2020). In-
 228 stead, here we focus on MAVEN data of the undisturbed IMF that describes solar wind
 229 activity at Mars; this allows us to investigate how changes in the IMF are seen at the
 230 surface and how much the presence of the ionosphere influences the signal. We use data
 231 in the IMF during the time of InSight operations compiled by Halekas et al. (2017), to
 232 allow e.g., joint investigations of the solar rotations (Carrington cycles) in MAVEN and
 233 IFG data. The resulting time series comprises distinct intervals during the MAVEN mis-
 234 sion when part of MAVEN’s orbit was in the solar wind. MAVEN data is shown in Mars
 235 Solar Orbit (MSO) frame in which x points from Mars towards the Sun, y points anti-
 236 parallel to Mars’ orbital velocity vector and z completes the right-handed system.

237 4 Surface Observations of Time-varying Magnetic Fields

238 We discuss transient and periodic external fields observed at the surface starting
 239 with a few seconds up to the longest period observable with InSight data, a Martian year
 240 (Table 1 and Figure 4). The dominant signal in the power spectral density (PSD) at the
 241 surface is the daily period and its harmonics. Shorter-period ULF waves, ranging from
 242 seconds to minutes occur intermittently and are seen in the PSD if time intervals with
 243 such occurrences are selected accordingly. The PSD falls off as $\sim 1/f$ for periods of a day
 244 and shorter as predicted from satellite data and used in noise models for InSight seis-
 245 mometer operations (Mimoun et al., 2017). Despite the data gaps, the more than one
 246 martian year of observations now constitutes several solar rotation periods, and although
 247 weak compared with the diurnal peak (Figure 4), an ~ 26 -day spectral signature is ob-
 248 served which is discussed further later (section 4.4). One full annual cycle allows iden-
 249 tification of seasonal variations, although thorough analysis of seasonal and longer pe-
 250 riodicities would require measurements for several years. In the following, we discuss In-
 251 Sight observations of transient and then periodic phenomena separating aspects that have
 252 been reported previously from new observations.

253 4.1 Previous Observations of Local Dust Movement

254 Dust is ubiquitous on Mars and can affect the planet globally or regionally via sea-
 255 sonal dust storms, but also locally via transient phenomena like dust devils in which cy-
 256 clostrophic motion of triboelectrically charged dust behaves as a magnetic solenoid (Farrell,
 257 2004; Kurgansky et al., 2007). Dust-carrying vortices, or dust devils, are common on Mars
 258 and the dust columns and/or their tracks have been captured by cameras of earlier sur-
 259 face and orbital missions as early as Viking (Balme & Greeley, 2006; Thomas & Gierasch,
 260 1985).

261 So far InSight has not imaged any dust devils directly (Banfield et al., 2020; Lorenz
 262 et al., 2021), but orbital observations of linear tracks suggest dust devil activity at the
 263 InSight landing site (Perrin et al., 2020). Further, local dust movement identified around
 264 the InSight landing site was investigated with multiple instruments on InSight and Charalambous
 265 et al. (2021) focused on a small number of individual events for which dust transport was
 266 evident from consecutive images. Associated magnetic field changes were possibly de-
 267 tected, however, it was somewhat unclear if observed signals were actually driven by dust
 268 movement.

269 To investigate this further, Thorne et al. (2022) systematically analyzed magnetic
 270 field signals during catalogued pressure drops (Spiga et al., 2021) known to be result of
 271 passing dust devils. They found that only few events ($\sim 8\%$) show a significant signal at
 272 the time of pressure drops in any component. Most of the time magnetic field signals dur-

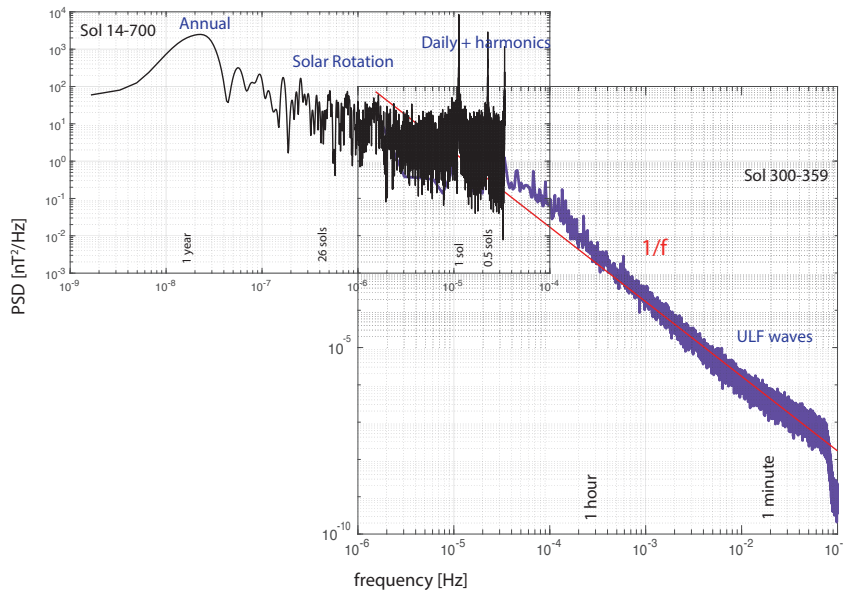


Figure 4. Power spectral density (PSD) for the surface magnetic field strength at the In-Sight landing site. PSD estimates for longer periods are derived using a Lomb-Scargle algorithm (black). For shorter periods (purple) a Welch spectrum was used for data from sols 300-359, a time period without large data gaps. The composite spectrum is motivated by Figure 2 in (Constable, 2007) showing an equivalent representation for the Earth.

273 ing a pressure drop are small, and similar to the background magnetic field. The origin
 274 of signals when observed was also investigated. Three mechanisms were explored: land-
 275 er or ground tilt, solar array current generated fields, and triboelectric effects. Only the
 276 latter was found to reach observed magnitudes (>0.3 nT) in the case of exceptionally
 277 large dust devils. This is a possible explanation for the rare observations of dust devil
 278 magnetic field signatures and direct visual observations.

279 4.2 Space Weather

280 4.2.1 Previous Observations

281 InSight has been operating on Mars during quiet conditions of the solar cycle and
 282 little space weather has occurred so far. However, a corotating interaction region (CIR)
 283 hit Mars on December 8 and Sol 723, followed by a coronal mass ejection (CME) two
 284 sols later on December 10 and Sol 725 (Mittelholz, Johnson, Fillingim, et al., 2021). De-
 285 tailed description of observations in Mittelholz, Johnson, Fillingim, et al. (2021) show
 286 the effect on the martian magnetic field at the surface and we summarize the two main
 287 findings to provide context for additional observations from 2022. First, although there
 288 was no clear onset of the CME or CIR, increased peak-to-peak (P2P) amplitudes in the
 289 diurnal variations were visible in all components, especially in the early to mid morn-
 290 ing compared to prior sols. Magnetic field changes were seen for several days starting
 291 approximately 2 sols before the CIR peak hit and lasted until approximately 2 sols af-
 292 ter the CME peak arrival. Second, we observed fluctuating fields with periods of tens
 293 of minutes to a few hours dominantly in the B_{East} but also in the other components dur-
 294 ing the night-time. Those mostly followed the CME.

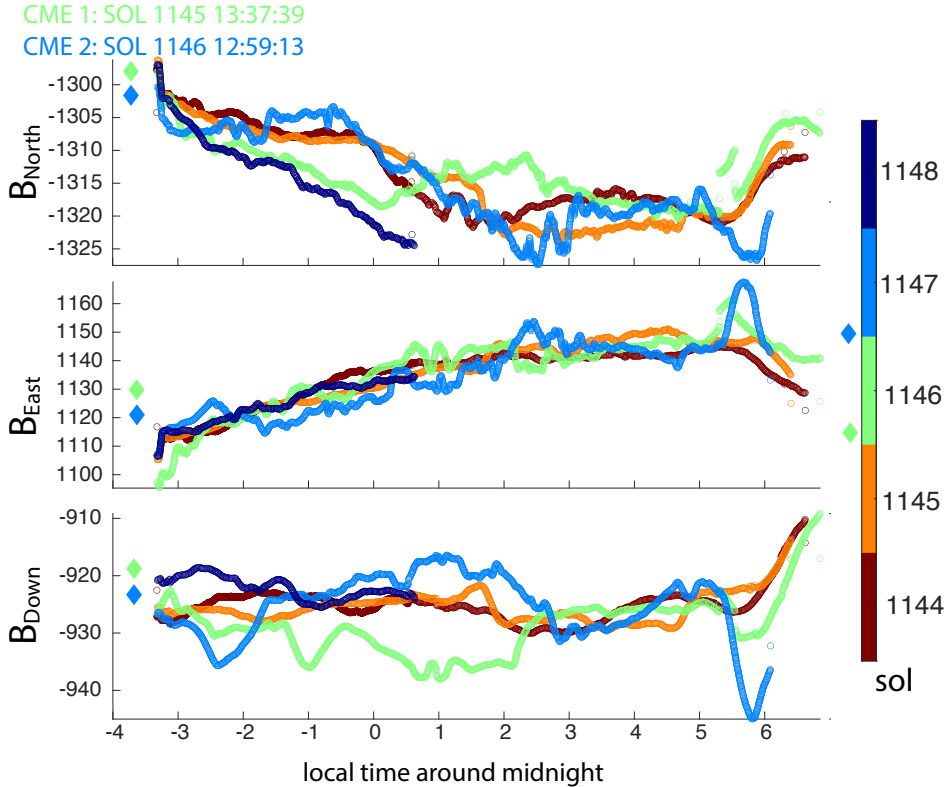


Figure 5. Effects of two CMEs from sols 1145 and 1146 (February 15-16, 2022): The 3 components of the magnetic field color coded by night. The x-axis is local time around midnight. The CMEs encountered Mars during the day on the sols marked by the colored diamonds, but there is no day-time IFG data for those sols.

295

4.2.2 New Observations

296

297

298

299

300

301

302

303

304

305

306

On February 15-16 2022, two further CMEs encountered Mars at times when the IFG was fortuitously switched on during the night-time (Figure 5). The events were weak and did not directly impact the planet, but Mars was magnetically connected to the CME flanks (see supplementary GIF). MAVEN was not in the solar wind at the time of the events, but the Solar energetic particle (SEP) instrument saw an increase in ion and electron energies. Additionally Solar Wind Ion (SWIA) and Electron Analyzer (SWEA) detect increased fluxes indicative of a compressed magnetosphere (see SFigure 1). Although the lack of day-time data does not allow investigations of the diurnal P2P signal, night-time fluctuations are again evident in the data. Although the CMEs occurred in the early afternoon on sols 1145 and 1146, we observed fluctuations on the order of 30 mins in the field lines for the following nights, similar to the events from December 2020.

307

308

309

310

311

312

313

314

315

In order to investigate the impact of solar wind activity on surface-based observations more generally, we made use of an orbit-averaged proxy for the upstream solar wind data for times when MAVEN is not in the solar wind (Halekas et al., 2017). We use this to investigate whether the diurnal P2P amplitude recorded by the IFG was affected by solar wind conditions as measured or inferred from the MAVEN plasma particle instrument suite. We focus on solar wind dynamic pressure, $P_{dyn} = \rho v^2$, and IMF amplitude, B , and evaluate an P_{dyn} and B per InSight sol; for sols where more than 1 orbit in the solar wind is available, we average all orbits per sol. A correlation between P_{dyn} and B is seen for MAVEN data in Figure 6a and we use those as proxy for solar wind activ-

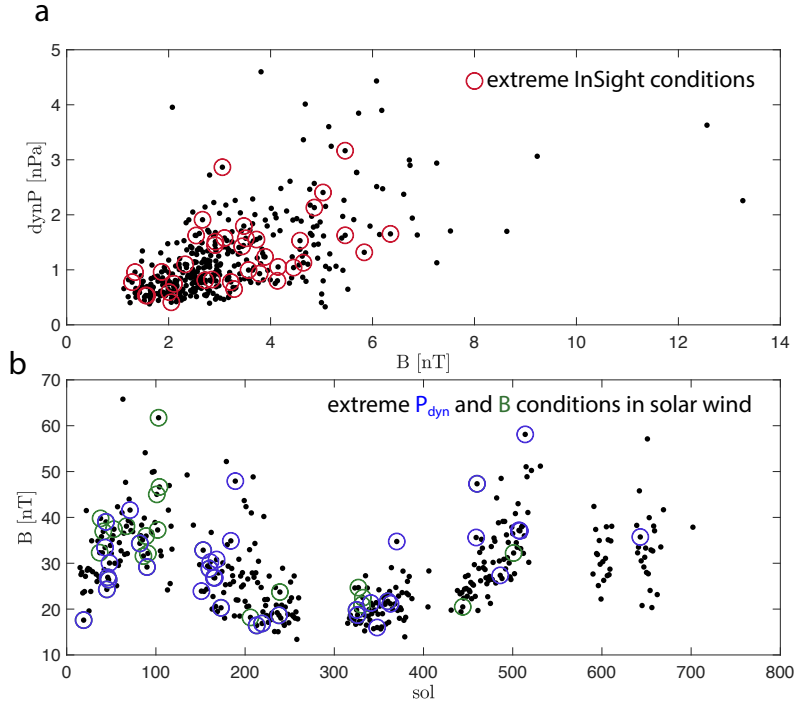


Figure 6. (a) MAVEN solar wind dynamic pressure, P_{dyn} , vs. the IMF amplitude, B , measured upstream of the bowshock. The red circles indicate days on which InSight’s P2P amplitude is larger than on 90% of the sols. (b) InSight P2P amplitude versus sol. Sols with extreme (defined as highest 10%) P_{dyn} (blue) or B (green) are highlighted.

316 ity; however, the largest 10% of P2P amplitudes in the InSight data do not coincide with
 317 days of either proxy for high solar wind activity. Similarly, we find that InSight diurnal
 318 P2P values are uncorrelated with extreme P_{dyn} or B conditions (Figure 6b) with cor-
 319 relation coefficients of 0.02 and 0.03 respectively.

320 Overall, at least during the quiet phase of a solar cycle, magnetic signatures of so-
 321 lar activity at the martian surface are limited. Although during weak to moderate space
 322 weather events an increase in the diurnal P2P magnetic field amplitude is visible, it oc-
 323 curs gradually and the effect is not immediately obvious. An avenue of further investi-
 324 gation could be a focus on short period waves, which are visible during the night (Sec-
 325 tion 4.6) and thus during times at which less activity is expected from other sources such
 326 as the ionosphere or lander generated fields.

327 4.3 Seasonal

328 4.3.1 Previous Observations

329 We previously examined variations of the diurnal pattern for the first 389 sols on
 330 Mars and found that peak daily amplitudes vary throughout the mission and with sea-
 331 son (Mittelholz, Johnson, Thorne, et al., 2020). Despite the incomplete annual cover-
 332 age at that point, dust and seasonal variability of the atmosphere seemed to lead to vari-
 333 ability in wind-driven ionospheric currents. Larger P2P amplitudes were found for the
 334 beginning of the mission occurring during the winter with a peak coinciding with a global
 335 dust storm, starting around sol 45 (Figure 7). We used a Mars Global Circulation Model
 336 (Forget et al., 1999; González-Galindo et al., 2013) to simulate expected ionospheric cur-

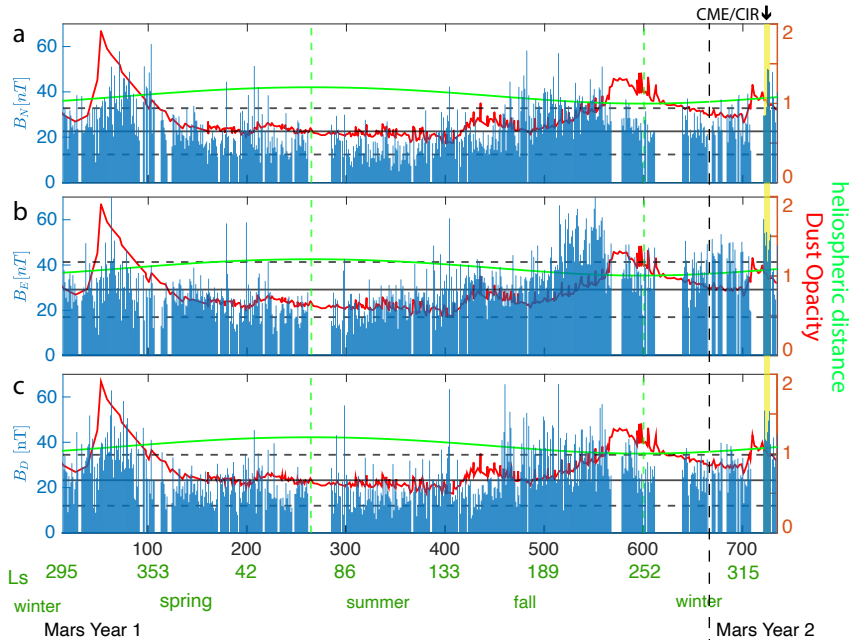


Figure 7. Peak-to-peak amplitude of B_N , B_E and B_D between 05:00 and 10:00 TLST (left y-axis) and the median (solid) value ± 1 standard deviation (dashed). Heliospheric distance in AU (green) and dust opacity (red) (right y-axis).

337 rents and the resulting surface magnetic fields mainly driven by predicted seasonal vari-
 338 ations in electron density and neutral wind velocity, and assuming end-member cases for
 339 ionospheric current geometries, a line and sheet current. We estimated nominal seasonal
 340 variations in atmospheric parameters and dust storm scenarios for the dust season (Mittelholz,
 341 Johnson, Thorne, et al., 2020). The model bounds predicted by atmosphere driven fields
 342 were consistent with InSight observations. A further study decomposed magnetic field
 343 variations into their natural orthogonal components (Luo et al., 2022) and found that
 344 the first eigenmode corresponded to atmospheric variations confirming the ionosphere
 345 as primary driver of magnetic variability.

346 4.3.2 New observations

347 We perform an updated analysis of the diurnal maximum amplitudes using con-
 348 tinuous data and MGCM predictions extending just over a full martian year, thus cov-
 349 ering all seasons. As previously, we restrict our analysis to days for which more than 80%
 350 of the data are available and because we compare MGCM predictions for wind-driven
 351 magnetic fields Mittelholz, Johnson, Thorne, et al. (2020) with a 26-sol running mean
 352 of the maximum diurnal values, we only keep data for which the running mean includes
 353 at least 50% of the sols (13 sols). The results confirm the overall agreement between the
 354 observed and predicted field amplitudes (Figure 8). The observed magnetic field at times
 355 of dust storms (defined as times where dust opacity > 1) around sol 50-100, 540-620 and
 356 710-725 follows the modelled predictions during dust storms well. In general, i.e. not only
 357 focused on dust storm seasons, the daily magnetic field P2P amplitude correlates with
 358 dust opacity, which further corroborates the important effect of the atmosphere on mag-
 359 netic field observations (Figure 7 and 9b).

360 Further, we observe that diurnal peak-to-peak (P2P) variability throughout the mis-
 361 sion is broadly anticorrelated with heliospheric distance, with lowest P2P amplitudes oc-

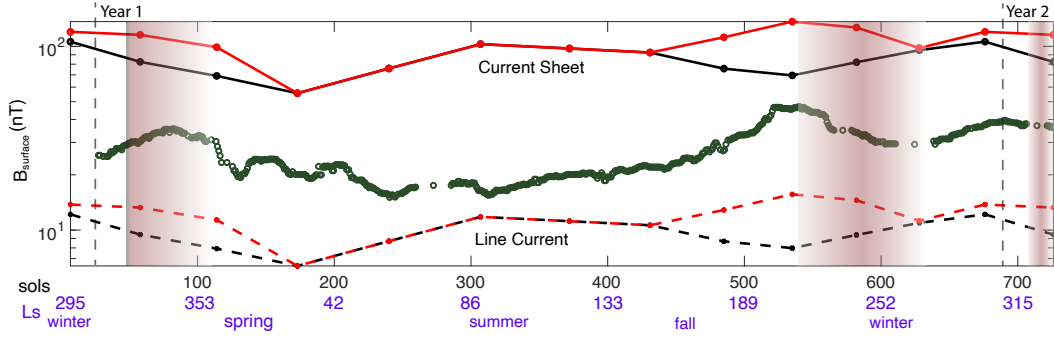


Figure 8. Wind-driven magnetic field response, $|B|$, at the surface assuming that the ionospheric dynamo current is a line current (dashed line) or a current sheet (solid line). The black line shows the prediction for an average scenario for atmospheric conditions; the red line shows the prediction for a seasonal dust storm scenario. The brown areas highlight times during which regional dust storms occurred during the InSight mission (defined as opacity larger than 1). The green curve shows the maximum amplitude of the observed magnetic field in a 26-sol running window for comparison with wind-driven predictions.

362 curring near aphelion or northern hemisphere summer (Figure 7 and 9a). However, the
 363 $1/r$ dependence of B seen at satellite altitudes (Mittelholz et al., 2017) is not seen
 364 on the ground.

365 Atmospheric parameters and IMF field strength both vary seasonally, and disen-
 366 tangling their effects is not fully possible. A larger ambient draped magnetic field at per-
 367 helion in the martian winter likely affects the dynamo region and enhances ionospheric
 368 fields. However, based on Figure 9 and the lack of clear correlation between solar wind
 369 parameters and the magnetic field (Section 4.2), atmospheric variations and the iono-
 370 sphere seem to be the dominant drivers of the diurnal surface magnetic field variations.
 371 We conclude that currents depending on electron density, temperature and horizontal
 372 wind velocity within the ionospheric dynamo region and dust in the atmosphere are the
 373 main driver of seasonally varying P2P amplitudes in the surface magnetic field at InSight.

374 4.4 Carrington Rotation

375 4.4.1 Previous Observations

376 As mentioned, a study investigated sources of observed variability including the syn-
 377 odic Carrington period of ~ 26.4 days (25.6 sols) by decomposing IFG magnetic field vari-
 378 ations into their natural orthogonal components (Luo et al., 2022). The first eigenmode
 379 was shown to correspond to atmospheric variations, and spectral properties of the sec-
 380 ond to fifth eigenmodes resulted in a peak expected for Carrington rotations, and were
 381 thus interpreted to be driven by variations in the draped IMF.

382 4.4.2 New Observations

383 It has been challenging to observe the average synodic Carrington period in IFG
 384 data because of data gaps and the limited total duration of observations. The approx-
 385 imately one martian year of continuous data comprises ~ 26 Carrington cycles, with mul-
 386 tiple substantial data gaps (Figure 2). Here we use the Lomb-Scargle periodogram which
 387 is particularly suited to time series with gaps and estimates the power spectrum by di-
 388 rectly least-square fitting to sinusoids at specified frequencies (VanderPlas, 2017).

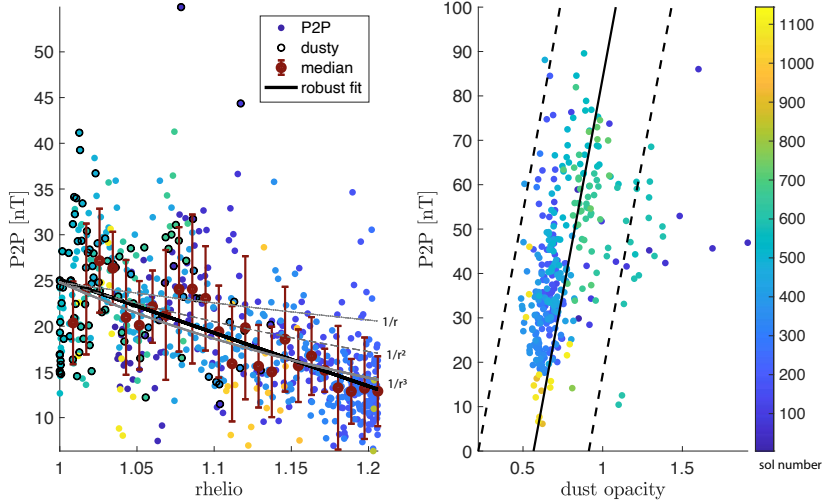


Figure 9. (a) P2P amplitudes vs. Mars distance to the Sun (normalized by minimum distance) color coded by sol number. Dark red circles and error bars represent median and standard deviation in heliospheric distance bins. Red outlined data points correspond to sols on which dust opacity is larger than 0.8. (b) P2P amplitude vs. dust opacity with a linear fit.

389 The Carrington period and harmonics are observed clearly in orbital data (Figure
 390 10 a,b) during the time interval of InSight operations. MAVEN magnetic field data taken
 391 in the undisturbed solar wind (Halekas et al., 2017) show a dominant peak at 26.1 sols
 392 with additional peaks of reduced amplitude. One is at about 13 sols and likely reflects
 393 the first harmonic, the physical origin of others is unclear. The WIND spacecraft shows
 394 a spectral peak at slightly longer periods of 27 sols (note that this is given in sols for bet-
 395 ter comparison) at the same approximate time periods as MAVEN (Figure 10a). This
 396 shift is expected because of the longer synodic Carrington period at Earth c.f. Mars.

397 The extent to which the Carrington cycle is observed in different magnetic field com-
 398 ponents depends on the position of the planet in the Parker spiral (see Section 2). Sim-
 399 ilar power is observed in WIND data in B_x and B_y because the IMF is directed more
 400 radially outward at this heliocentric distance. In contrast, MAVEN data taken in the undis-
 401 turbed IMF (Figure 10b), show little power in the B_x component, but a very dominant
 402 peak in the horizontal B_y .

403 We analyze InSight’s spectral content in the Mars body-fixed frame (MBF) because
 404 any residual field that is static in the MBF frame will have time-varying signal in Mars
 405 Solar Orbital (MSO) frame. Two dominant peaks around 26 and 27.6 sols are observed
 406 and some other shorter period peaks, at 22 and 24.8 sols, are comparable to those ob-
 407 served in MAVEN data. However, different relative amplitudes for both orbital and sur-
 408 face data are observed. Additionally, the vertical power spectral density component (B_D)
 409 at InSight is dominant while a draped field geometry would affect horizontal components
 410 as seen in Mars orbital data. A possible reason for the dominant peak in the vertical com-
 411 ponent for IFG data is the following: The direction of currents in the ionosphere is in-
 412 fluenced by the geometry and the strength of the background magnetic field. Gradients
 413 in the background magnetic field, e.g., from lateral variations in magnetization of the
 414 crust, lead to gradients in ionospheric (Peterson and Hall) conductivity which in turn
 415 lead to localized spatial structure in currents. At the edge of such a current system a strong
 416 vertical magnetic field component is produced. Because the IMF leads to fluctuations

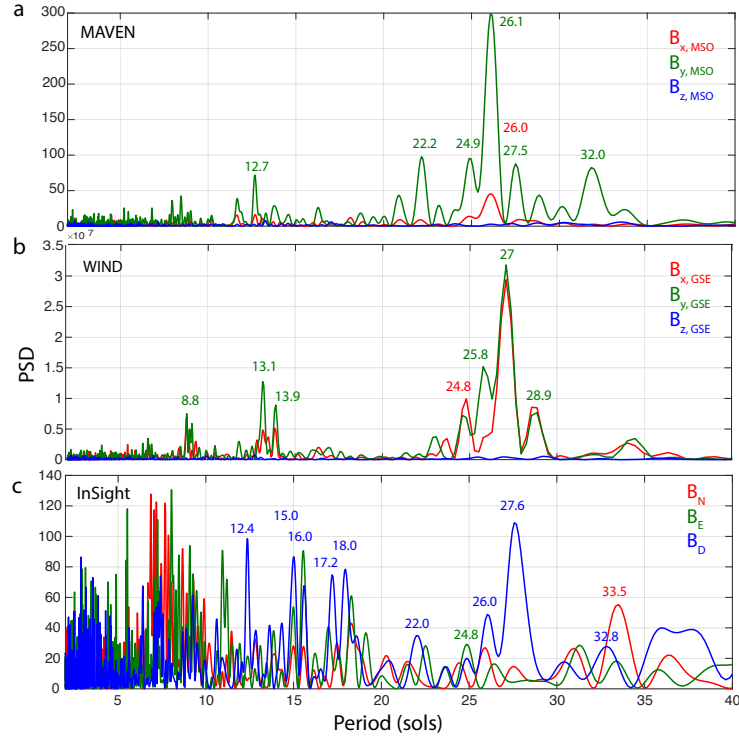


Figure 10. The power spectral density for (a) MAVEN in the undisturbed IMF at Mars (b) and WIND in the solar wind at Earth between December 2018 and October 2020. (a,b) are in the Mars Solar Orbit and Geocentric Solar Ecliptic, in both frames \hat{X} points towards the Sun and \hat{Z} is perpendicular to the plane of the planet’s orbit around the Sun. (c) InSight data is shown in Mars Body Fixed Frame. Note that periods shorter than 2 sols are excluded. Prominent peaks are marked in colors indicating the corresponding component.

417 of the current system itself (Brain et al., 2003; Mittelholz et al., 2017), the contribution
 418 of this vertical magnetic field has the periodicity of the IMF. At the InSight landing site
 419 the strength of the crustal magnetic field in the dynamo region is ~ 50 nT (Figure 5 in
 420 Mittelholz, Johnson, Thorne, et al. (2020)), and observed external field fluctuations are
 421 of similar magnitude (Figure 6 in Mittelholz, Johnson, Thorne, et al. (2020)). In this con-
 422 figuration, crustal fields that rotate below the ionosphere dynamically interact with iono-
 423 spheric fields. Hence, this hypothesis implies that observations of Carrington rotations
 424 would affect different components of the magnetic field depending on strength and di-
 425 rection of the crustal magnetic field around the site of measurement.

426 **4.5 Daily and Harmonics**

427 **4.5.1 Previous Observations**

428 The diurnal variations in IFG data observed up to sol 389 have been discussed in
 429 detail (Mittelholz, Johnson, Thorne, et al., 2020). Peak amplitudes of up to 70 nT were
 430 observed and on average the largest amplitude and variability was observed in B_E and
 431 the early-to mid-morning peak.

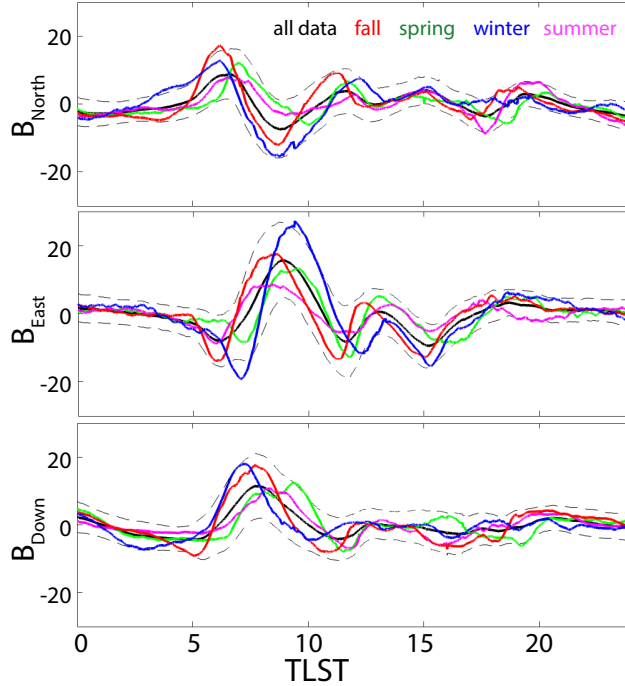


Figure 11. The 3 components of the detrended magnetic field averaged in 10000 local time bins for data within 30 degrees solar longitude of solstices and equinoxes and averaged over the all available full sol data (black) with one standard deviation uncertainty (dashed).

432

4.5.2 New Observations

433

434

435

436

437

438

439

440

441

Here we extend the analysis to include a full martian year, analyzing the 3 components of the magnetic field as a function of local time separated by season and averaged over all complete sols (Figure 11). Winter sols exhibit the largest P2P amplitude in B_{East} and the early morning. Smaller annual variability is seen during other times of the day. While summer sols show smallest P2P amplitudes (Figure 3, 7), the early morning peak still reaches the highest amplitude. As discussed before, the early morning peak coincides with times at which the product of electron density and horizontal wind velocity peaks and this effect is most pronounced during the winter; this suggests that the pattern is at least partially driven by ionospheric currents.

442

4.6 Short period waves

443

4.6.1 Previous Observations

444

445

446

447

448

449

450

451

452

453

454

Ultra low frequency (ULF) waves have repeatedly been observed since the first sol of IFG observations (Chi et al., 2019; Johnson et al., 2020). Known phenomena falling into this frequency range include pulsations, but also transient signals as discussed above and artificial noise, e.g., due to the solar array currents. InSight observations of pulsations with periods between seconds and minutes, likely result from the solar wind interacting with the martian magnetosphere, e.g., oscillations of the induced magnetosphere flanks or of the magnetotail (Chi et al., 2019). One example of an early ULF observation at night from sol 37 to 38 (Figure 12) shows power in the horizontal components from a few mHz to ~ 50 mHz, that builds and peaks around 2 am, with virtually no power in the vertical component in this frequency band. The signal bandwidth increases as the signal amplitude increases (Figure 12a-c). Small spikes in the data (broad-band and short-

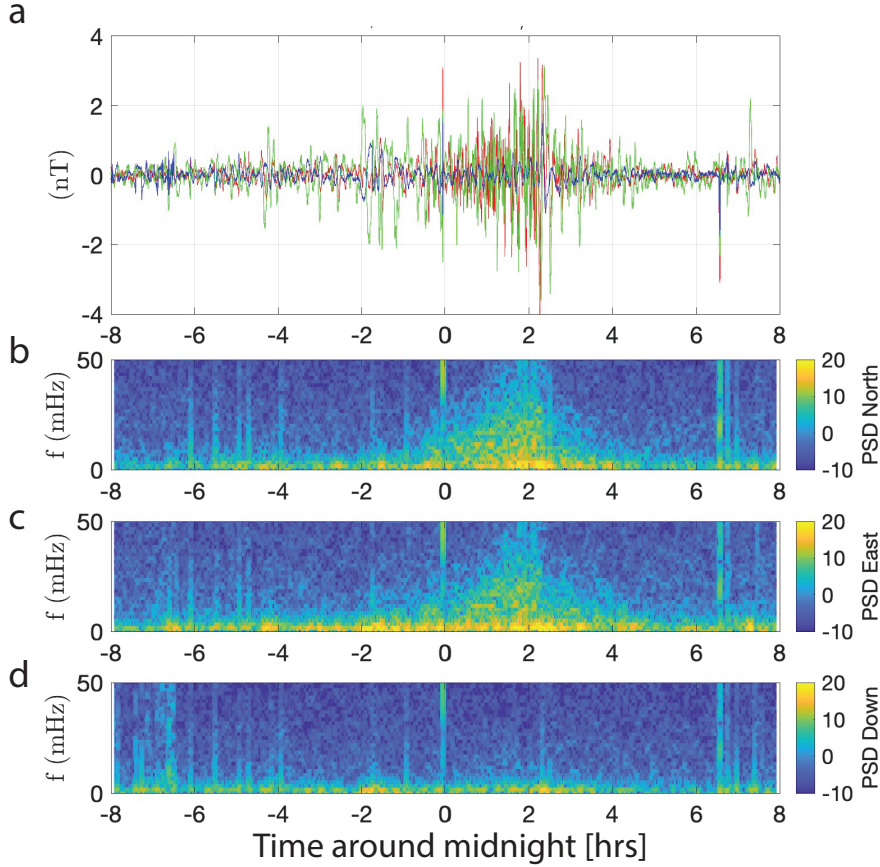


Figure 12. Wave activity on sol 37-38 / January 4-5, 2019. (a) Magnetic field components B_{North} (red), B_{East} (green) and B_{Down} (blue), detrended with a 20 minutes running mean. (b-d) Power spectral density for B_{North} , B_{East} and B_{Down} , respectively.

455 duration in the frequency domain), notably at midnight, are the result of lander activ-
 456 ity.

457 **4.6.2 New Observations**

458 Next we focus on observations of waves in the 1-50 mHz frequency range through-
 459 out the continuous time series at the surface irrespective of their origin. Guided by the
 460 observations of individual occurrences of waves, (e.g., Figure 12), we calculate the root-
 461 mean-square (RMS) amplitude of the bandpass power in 3 frequency bands: 1 - 5 mHz,
 462 5 - 20 mHz and 20 - 50 mHz (Figure 13). Especially, for the 1 - 5 mHz range, we observe
 463 ULF waves typically around midnight, and at dusk/dawn (Figure 12a). This occurrence
 464 is consistent with waves driven by an oscillating magnetosphere, i.e., pulsations, because
 465 during the daytime the ionosphere likely shields the lower atmosphere, preventing waves
 466 from travelling to the surface (see Figure 13a). Increased amplitudes between sunrise and
 467 sunset in all frequency bands are observed and are dominated by spacecraft contribu-
 468 tions. The high amplitude signal before noon in the 1 - 5 mHz band is associated with
 469 the time at which solar arrays typically reach their full charge after which the solar ar-
 470 ray currents drop rapidly. Similarly to the magnetic field amplitude (Figure 3), we see
 471 substantial sol-to-sol variability and seasonal dependence. For example, in the 1 - 5 mHz

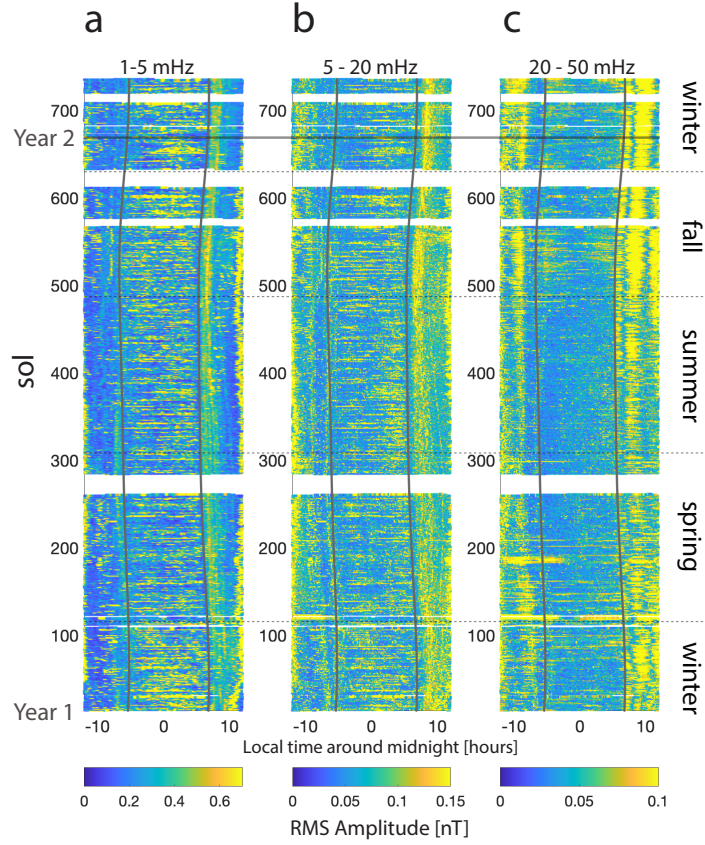


Figure 13. Bandpass power of B_{East} up to sol 732 for the frequency range of 1-5 mHz (200-1000 seconds), 5-20 mHz (50-200 seconds) and 20-50 mHz (20-50 seconds) The grey lines indicate the time of sunrise and sunset.

472 band, the nighttime amplitudes prior to sol 100 and after sol 500 is larger, correspond-
 473 ing to the northern hemisphere fall and winter. In the two higher frequency bands lander-
 474 related signals mask most natural wave activity during the day-time (see Figure 13b,c).
 475 During the night, the 5 - 20 mHz band shows similar characteristics to the 1 - 5 mHz
 476 band, but the duration of the signals is shorter, consistent with the observations in Fig-
 477 ure 12b,c. In the highest frequency range (20 - 50 mHz), day-time noise is prevalent, and
 478 night-time RMS amplitudes are small and of short duration.

479 4.7 Challenges

480 Lastly, we point out some of the challenges that result from the lack of a dedicated
 481 cleanliness program for the IFG. In particular, we caution extensive use of the diurnal
 482 pattern and its harmonics due to difficulties in differentiating separating natural and
 483 artificial signals on diurnal time scales at the few nT level. We list important aspects that
 484 can guide further use of IFG data, but we note that the results reported here are robust
 485 with respect to these issues (Joy et al., 2019; Johnson et al., 2020; Mittelholz, Johnson,
 486 Thorne, et al., 2020; Thorne et al., 2020).

- 487 • Separation of the diurnal signal from natural and artificial sources has been dis-
488 cussed in (Mittelholz, Johnson, Thorne, et al., 2020; Thorne et al., 2020) in de-
489 tail. Challenges are related to diurnal fluctuations in temperature and solar ar-
490 ray currents, both of which result in peak signals during the daytime, when naturally-
491 occurring (ionospheric or draped-IMF-related) diurnal signals are also expected
492 to be a maximum. Calibration efforts aim to remove artificial signals (Joy et al.,
493 2019), however, solar array currents are sampled sparsely and the temperature gain
494 does not behave linearly.
- 495 • Further, temperature-driven effects are enhanced in the B_x component compared
496 to B_y and B_z (Joy et al., 2019). This is of particular importance for studies in which
497 the ratio of power in different components (e.g. vertical vs. horizontal) is evalu-
498 ated (see Section 5.1).
- 499 • Small signals such as those that might occur in association with dust devils (i.e.,
500 <0.5 nT), can be obscured by high frequency solar array current fluctuations. This
501 is shown in (Thorne et al., 2022) and can bias the local times at which small nat-
502 urally occurring signals can be detected.
- 503 • Although lander activity is usually easily identified (Mittelholz, Johnson, Thorne,
504 et al., 2020), automated processing that leads to the calibrated data products on
505 the PDS do not always fully remove such signatures, in particular those with step-
506 like characteristics. Those artifacts affect the full band-width which complicates
507 automatic detection of signals such as short period waves.
- 508 • Data gaps (Figure 2 and 3) throughout the mission lead to incomplete time se-
509 ries and challenges associated with spectral analysis. The Lomb-Scargle algorithm
510 applied in this paper can mitigate this issue.

511 5 Implications

512 5.1 Magnetic Sounding

513 Time-varying magnetic fields are of particular interest for studying the interior elec-
514 trical conductivity structure of a planet. Here one relies on the fact that time-varying
515 fields induce eddy currents in the subsurface that in turn produce measurable secondary
516 magnetic fields. The electrical conductivity can be determined from the secondary fields.
517 Electrical conductivity is an intrinsic material property dependent on temperature and
518 composition (Constable, 2007) and so it is complementary to other geophysical inves-
519 tigations.

520 Separation of the primary (inducing) from secondary (induced) fields to determine
521 electrical conductivity requires information beyond data from a single magnetometer.
522 In classical geomagnetic sounding (e.g. (Banks, 1969)), the primary field geometry is as-
523 sumed to be a dipole formed from Earth’s ring current (which in turn is manifested from
524 the strong intrinsic dipole field). Signals spanning many decades in frequency are all con-
525 strained by the same simple geometry. The theory relates the vertical field to the hor-
526 izontal gradients of the horizontal fields through a frequency-dependent inductive length
527 scale or penetration depth that varies with electrical conductivity (Olsen, 1999). Because
528 the gradients are computed analytically, the ratios of vertical to horizontal fields can be
529 used directly, hence this method is also called the Z/H technique. Similarly, Mittelholz,
530 Grayver, et al. (2021) estimated the electrical conductivity of the Moon assuming that
531 the source field in Earth’s magnetotail followed a dipole.

532 In spite of a strong degree-one (day-night) signal in Mars’ ionospheric variation,
533 attempts at geomagnetic sounding have not been successful. Multipole analysis has been
534 similarly inhibited, although comparable efforts using Earth’s solar-quiet (Sq) ionospheric
535 variations have enjoyed limited success (Bahr & Filloux, 1989). The geometry of iono-
536 spheric variations on Mars have been studied using satellites (Section 2), but their spa-
537 tial structure is still complex and not easily explained by a simple geometry, i.e. only

538 a specific subset of Gauss coefficients. Specifically for InSight data, several challenges
 539 have become apparent to derive electrical conductivity (Mittelholz, Johnson, Grimm, et
 540 al., 2020). First, the relationships between vertical and horizontal components do not
 541 follow poloidal-induction theory and further diurnal signals in particular remain suspect
 542 because of contamination from spacecraft fields (see section 4.7).

543 Additional measurements could circumvent the dependency on assumed geometry
 544 and resolve these issues. Horizontal field gradients can be directly estimated using a mag-
 545 netometer array (Gough & Ingham, 1983). This was the approach proposed for Netlander
 546 (Pinçon et al., 2000). The magnetic transfer function between orbiting and landed space-
 547 craft was used successfully for the Moon (Sonett (1982) for a review) but Mars’ inter-
 548 vening ionosphere appears to reduce coherence. Alternatively, the magnetotelluric method
 549 (e.g., Vozoff (1991)) measures the time-varying electric field at the surface in addition
 550 to the magnetic field. This is a complete single-station sounding that only weakly de-
 551 pends on source geometry (R. E. Grimm & Delory, 2012) and is currently in develop-
 552 ment for planetary missions (R. Grimm et al., 2021).

553 5.2 Future Observations

554 InSight’s magnetometer has enabled a range of observations of time-varying mag-
 555 netic fields at the landing site, over a time frame of more than one martian year. Includ-
 556 ing magnetometers on future missions at a variety of locations and thus extending the
 557 spatial distribution and time span of such observations will be of great value in under-
 558 standing a range of phenomena:

- 559 1. Above we discuss the crustal magnetic field interacting with the IMF and iono-
 560 spheric currents. While the above discussion is motivated by InSight results and
 561 thus a unique crustal magnetic field setting, the influence of crustal magnetiza-
 562 tion on the ionosphere could be tested under different field geometries and am-
 563 plitudes.
 564 For example, for the spectral content at the 26-sol period, we suggest that power
 565 partitioning among the different field components at InSight results from the crustal
 566 magnetic field geometry interacting with the ionosphere (section 4.4). Following
 567 the same argument, we predict that at a different landing site, with weaker or no
 568 crustal fields affecting ionospheric currents, a diurnal signal in mainly the hori-
 569 zontal components would be expected. Large-scale strong magnetic fields above
 570 the instrument (as observed in regions such as Terra Cimmeria / Sirenum) would
 571 likely also lead to a horizontally dominant peak reflecting compression and exten-
 572 sion of closed crustal fields due to varying magnetic pressure.
 573 Further, the geometry of the crustal magnetic field at the landing site influences
 574 local ionospheric conductivity and the dynamo region directly. A different back-
 575 ground field would thus lead to a different magnetic field environment (Lillis et
 576 al., 2019; Fillingim et al., 2012).
- 577 2. At other mission landing sites such as those of Spirit, Curiosity or Perseverance,
 578 multiple dust devil images provide evidence for dust being lofted while this ob-
 579 servation has not been made with InSight. It is thus not clear if the paucity of mag-
 580 netic field signals at the times of pressure vortices simply reflects a lack of dusty
 581 vortices. If there was dust lofted more readily, could we frequently observe signals
 582 associated with pressure drops?
- 583 3. The solar cycle is currently in its ascending phase and will peak in 2026, while the
 584 IFG has been operating during a quiet period. A longer time series covering a full
 585 solar cycle, especially during solar maximum, increases the probability of observ-
 586 ing large space weather events. Measuring the magnetic field response of such events
 587 at multiple sites would be particularly useful, especially if such observations were
 588 also made simultaneously by orbital spacecraft. In orbit, crustal field topology is

589 known to be affected by CMEs where in weak/strong crustal fields an increase in
 590 draped/open field lines is observed (Xu et al., 2019; Luhmann et al., 2017). Open
 591 crustal field lines can reconnect with solar wind field lines in a process called re-
 592 connection, leading to a direct connection of plasma environment to the surface.
 593 Direct access to the lower atmosphere and surface, leads to increased atmospheric
 594 escape (Xu et al., 2019; Luhmann et al., 2017) and radiation doses as shown by
 595 the radiation experiment on Mars Science Laboratory (Hassler et al., 2012). An
 596 additional instrument suite describing the plasma environment would further en-
 597 hance understanding of space weather effects at the surface, an important aspect
 598 for future human exploration efforts.

- 599 4. The limited duration of the IFG time series does not allow robust characteriza-
 600 tion of annual variability and long term trends. Installation of long-time obser-
 601 vatories on the surface of Mars would allow long-term tracking of magnetic vari-
 602 ability on Mars and better statistics on space weather events, as available on Earth.

603 6 Conclusion

604 InSight has offered us the first observations of time-varying magnetic fields as seen
 605 from the surface. We summarize observations ranging from periods of minutes to a year,
 606 and transient signals using data acquired during the entire mission, but focused on the
 607 first martian year. Transients include signals associated with local dust movement and
 608 space weather, periodic signals include ultra low frequency waves, diurnal signals, Car-
 609 rington rotations and seasonal variations. Major drivers of time-varying magnetic fields
 610 are ionospheric currents and direct solar wind interactions appear to be a secondary ef-
 611 fect. In particularly the effect of dust storms and seasonal variations on diurnal and shorter
 612 periods, and the overall correlation of peak diurnal amplitudes with dust opacity (Fig-
 613 ure 9) strengthens this hypothesis. Although the direct impact of the solar wind dur-
 614 ing space weather can be observed, producing peak diurnal amplitudes that are compa-
 615 rable to those at the times of dust storms (Fig 7), there is not direct correlation between
 616 solar wind activity and surface magnetic field observations. At the 26-sol period, the power
 617 in the vertical B_{Down} dominates, rather than the horizontal components that would be
 618 indicative of the draped IMF. This further corroborates an indirect effect of the IMF,
 619 i.e., the IMF likely affects the ionosphere leading to current systems which are ultimately
 620 observed on the ground.

621 The crustal magnetic field environment affects the geometry and amplitude of iono-
 622 spheric currents and observations of resulting magnetic fields are thus dependent on crustal
 623 magnetization at the landing site. Future magnetic field data acquisition at a variety of
 624 landing sites will thus shed further light on Mars' dynamic environment. The upcom-
 625 ing Exomars mission and its magnetometers will land in a rather strongly magnetized
 626 region and will provide a different perspective on crustal field line interaction with ex-
 627 ternal field fluctuations. China's Zhurong rover's landing site is in a region of weaker crustal
 628 field strength c.f. InSight (Langlais et al., 2019), potentially allowing investigations of
 629 some of the open issues raised above. This will allow studying the local nature and de-
 630 pendency on individual sites to the propagation of signals to the surface. Future explo-
 631 ration with low altitude platforms such as balloons or helicopters will open up even fur-
 632 ther possibilities in exploring multiple landing sites on a regional scale (Mittelholz et al.,
 633 2022; Bapst et al., 2021; Hall et al., 2007).

634 Acknowledgments

635 We acknowledge NASA, CNES, their partner agencies and Institutions (UKSA, SSO,
 636 DLR, JPL, IPGP-CNRS, ETHZ, IC, MPS-MPG) and flight operations team at JPL, SIS-
 637 MOC (SEIS on Mars Operations Center) and MSDS (Mars SEIS Data Service). We ac-
 638 knowledge support from Harvard's Daly Postdoctoral Fellowship (A.M.), the Natural Sci-

639 ences and Engineering Research Council of Canada (S.T., C.L.J) and the InSight Mis-
640 sion (C.L.J, S.J., M.F., S.S., W.B.). This research was carried out in part at the Jet Propul-
641 sion Laboratory, California Institute of Technology, under a contract with the National
642 Aeronautics and Space Administration (80NM0018D0004). This paper is InSight Con-
643 tribution Number 222.

644 **Open Research**

645 All InSight data used in this study is publicly available via the Planetary Data Sys-
646 tem at <https://doi.org/10.17189/1519202>. Data from the MAVEN mission are avail-
647 able via the Planetary Data System at [https://pds-ppi.igpp.ucla.edu/search/view/
648 ?f=yes&id=pds://PPI/maven.mag.calibrated/data](https://pds-ppi.igpp.ucla.edu/search/view/?f=yes&id=pds://PPI/maven.mag.calibrated/data). Upstream and proxy solar wind
649 data (Halekas et al., 2017) can be accessed at [http://www.physics.uiowa.edu/~jhalekas/
drivers.html](http://www.physics.uiowa.edu/~jhalekas/
650 drivers.html).

References

- 651
652 A Mittelholz, Johnson, C., Thorne, S., Chi, P., Fillingim, M., Joy, S., ... Banerdt,
653 W. (2022). The External Magnetic Field as Seen from InSight. *LPI Contributions*, 2678, 1242.
- 654
655 Acuna, M. H., Connerney, J. E. P., Ness, N. F., Lin, R. P., Mitchell, D., Carlson,
656 C. W., ... Cloutier, P. (1999). Global Distribution of Crustal Magnetization
657 Discovered by the Mars Global Surveyor MAG/ER Experiment. *Science*,
658 284(5415), 790–793. doi: 10.1126/science.284.5415.790
- 659 Bahr, K., & Filloux, J. H. (1989). Local Sq response functions from EMSLAB
660 data. *Journal of Geophysical Research: Solid Earth*, 94(B10), 14195–14200.
661 Retrieved from [https://agupubs.onlinelibrary.wiley.com/doi/abs/](https://agupubs.onlinelibrary.wiley.com/doi/abs/10.1029/JB094iB10p14195)
662 10.1029/JB094iB10p14195 doi: <https://doi.org/10.1029/JB094iB10p14195>
- 663 Balme, M., & Greeley, R. (2006). Dust devils on Earth and Mars. *Reviews*
664 *of Geophysics*, 44(3). Retrieved from [https://agupubs.onlinelibrary](https://agupubs.onlinelibrary.wiley.com/doi/abs/10.1029/2005RG000188)
665 [.wiley.com/doi/abs/10.1029/2005RG000188](https://agupubs.onlinelibrary.wiley.com/doi/abs/10.1029/2005RG000188) doi: [https://doi.org/10.1029/](https://doi.org/10.1029/2005RG000188)
666 2005RG000188
- 667 Banerdt, W. B., Smrekar, S., Banfield, D., Giardini, D., Golombek, M. P., John-
668 son, C., ... Wieczoreck, M. (2020). Initial Results from the InSight Mission
669 on Mars. *Nature Geoscience*, 13(March), 183–189. Retrieved from [http://](http://dx.doi.org/10.1038/s41561-020-0544-y)
670 dx.doi.org/10.1038/s41561-020-0544-y doi: 10.1038/s41561-020-0544-y
- 671 Banfield, D., Rodriguez-Manfredi, J. A., Russell, C. T., Rowe, K. M., Leneman, D.,
672 Lai, H. R., ... Team, T. T. (2018). InSight Auxiliary Payload Sensor Suite
673 (APSS). *Space Science Reviews*, 215(1), 4. Retrieved from [https://doi.org/](https://doi.org/10.1007/s11214-018-0570-x)
674 10.1007/s11214-018-0570-x doi: 10.1007/s11214-018-0570-x
- 675 Banfield, D., Spiga, A., Newman, C., Forget, F., Lemmon, M., Lorenz, R., ...
676 Banerdt, W. B. (2020). The atmosphere of Mars as observed by InSight.
677 *Nature Geoscience*, 13(March). Retrieved from [http://www.nature.com/](http://www.nature.com/articles/s41561-020-0534-0)
678 [articles/s41561-020-0534-0](http://www.nature.com/articles/s41561-020-0534-0) doi: 10.1038/s41561-020-0534-0
- 679 Banks, R. J. (1969). Geomagnetic Variations and the Electrical Conductivity of
680 the Upper Mantle. *Geophysical Journal International*, 17(5), 457–487. Re-
681 trieved from <https://doi.org/10.1111/j.1365-246X.1969.tb00252.x> doi:
682 10.1111/j.1365-246X.1969.tb00252.x
- 683 Bapst, J., Parker, T. J., Balaram, J., Tzanetos, T., Matthies, L. H., Edwards, C. D.,
684 ... Weiss, B. P. (2021). Mars Science Helicopter: Compelling Science En-
685 abled by an Aerial Platform. *Bulletin of the AAS*, 53(4). Retrieved from
686 <https://baas.aas.org/pub/2021n4i361> doi: 10.3847/25c2cfcb.a126aea0
- 687 Brain, D., Bagenal, F., Acuña, M. H., & Connerney, J. (2003). Martian magnetic
688 morphology: Contributions from the solar wind and crust. *Journal of Geophys-*
689 *ical Research*, 108(A12), 1424. Retrieved from [http://dx.doi.org/10.1029/](http://dx.doi.org/10.1029/2002JA009482)
690 2002JA009482 doi: 10.1029/2002JA009482
- 691
692 Brain, D., Bagenal, F., Acuña, M. H., Connerney, J. E., Crider, D. H., Mazelle, C.,
693 ... Ness, N. F. (2002). Observations of low-frequency electromagnetic plasma
694 waves upstream from the Martian shock. *Journal of Geophysical Research:*
695 *Space Physics*, 107(A6). doi: 10.1029/2000JA000416
- 696 Brain, D., Mitchell, D. L., & Halekas, J. S. (2006). The magnetic field draping
697 direction at Mars from April 1999 through August 2004. *Icarus*, 182(2),
698 464–473. Retrieved from [http://www.sciencedirect.com/science/](http://www.sciencedirect.com/science/article/pii/S0019103505004902)
699 [article/pii/S0019103505004902](http://www.sciencedirect.com/science/article/pii/S0019103505004902) doi: 10.1016/j.icarus.2005.09.023
- 700
701 Charalambous, C., McClean, J. B., Baker, M., Pike, W. T., Golombek, M., Lem-
702 mon, M., ... Banerdt, W. B. (2021). Vortex-Dominated Aeolian Activity at
703 InSight’s Landing Site, Part 1: Multi-Instrument Observations, Analysis, and
704 Implications. *Journal of Geophysical Research: Planets*, 126(6), 1–51. doi:
705 10.1029/2020je006757

- 706 Chi, P., Russell, C., Yu, Y., Joy, S., Ma, Y., Banfield, D., ... Banerdt, W. (2019,
707 dec). InSight Observations of Magnetic Pulsations on Martian Surface: Mor-
708 phology and Wave Sources. In *Agu fall meeting abstracts* (Vol. 2019, pp.
709 DI51B—0024).
- 710 Connerney, J. E. P., Espley, J. R., Dibraccio, G. A., Gruesbeck, J. R., Oliverson,
711 R. J., Mitchell, D. L., ... Jakosky, B. M. (2015). First results of the MAVEN
712 magnetic field investigation. *Geophysical Research Letters*, *42*, 8819–8827.
713 doi: 10.1002/2015GL065366
- 714 Constable, S. (2007). Geomagnetic induction studies. *Geomagnetism*, 237–276. Re-
715 trieved from <http://ci.nii.ac.jp/naid/10030366661/en/>
- 716 Crider, D., Vignes, D., Krymskii, A. M., Breus, T., Ness, N. F., Mitchell, D. L.,
717 ... Acuña, M. H. (2003). A proxy for determining solar wind dynamic
718 pressure at Mars using Mars Global Surveyor data. *Journal of Geophysical*
719 *Research*, *108*(A12), 1461. Retrieved from [http://dx.doi.org/10.1029/](http://dx.doi.org/10.1029/2003JA009875)
720 [2003JA009875](http://dx.doi.org/10.1029/2003JA009875){\%}5CnUsers/wang/GoogleDrive/Papers/2003JA009875.pdf
721 doi: 10.1029/2003JA009875
- 722 Espley, J. R., Cloutier, P. A., Brain, D. A., Crider, D. H., & Acuña, M. H. (2004).
723 Observations of low-frequency magnetic oscillations in the Martian magne-
724 tosheat, magnetic pileup region, and tail. *Journal of Geophysical Research:*
725 *Space Physics*, *109*(A7). doi: 10.1029/2003JA010193
- 726 Espley, J. R., Cloutier, P. A., Crider, D. H., Brain, D. A., & Acuña, M. H. (2005).
727 Low-frequency plasma oscillations at Mars during the October 2003 solar
728 storm. *Journal of Geophysical Research: Space Physics*, *110*(A9). Retrieved
729 from [https://agupubs.onlinelibrary.wiley.com/doi/abs/10.1029/](https://agupubs.onlinelibrary.wiley.com/doi/abs/10.1029/2004JA010935)
730 [2004JA010935](https://doi.org/10.1029/2004JA010935) doi: <https://doi.org/10.1029/2004JA010935>
- 731 Espley, J. R., Delory, G. T., & Cloutier, P. A. (2006). Initial observations of low-
732 frequency magnetic fluctuations in the Martian ionosphere. *Journal of Geo-*
733 *physical Research E: Planets*, *111*(6), 1–7. doi: 10.1029/2005JE002587
- 734 Farrell, W. M. (2004). Electric and magnetic signatures of dust devils from the
735 2000–2001 MATADOR desert tests. *Journal of Geophysical Research*, *109*(E3),
736 1–13. doi: 10.1029/2003je002088
- 737 Felici, M., Withers, P., Smith, M. D., González-Galindo, F., Oudrhiri, K., & Ka-
738 han, D. (2020). MAVEN ROSE Observations of the Response of the Martian
739 Ionosphere to Dust Storms. *Journal of Geophysical Research: Space Physics*,
740 *125*(6), 1–17. doi: 10.1029/2019JA027083
- 741 Ferguson, B. B., Cain, J. C., Crider, D. H., Brain, D. a., & Harnett, E. M.
742 (2005). External fields on the nightside of Mars at Mars Global Sur-
743 veyor mapping altitudes. *Geophysical Research Letters*, *32*(16), 1–4. doi:
744 10.1029/2004GL021964
- 745 Fillingim, M. O., Johnson, C. L., Mittelholz, A. M., Langlais, B., Russell, C. T.,
746 Joy, S. P. P., ... al., E. (2020). A first comparison between ionospheric and
747 surface level magnetic fields at Mars. *Earth and Space Science Open Archive*,
748 *14*. Retrieved from <https://doi.org/10.1002/essoar.10503286.1> doi:
749 10.1002/essoar.10503286.1
- 750 Fillingim, M. O., Lillis, R. J., England, S. L., Peticolas, L. M., Brain, D. A.,
751 Halekas, J. S., ... Bougher, S. W. (2012). On wind-driven electrojets at
752 magnetic cusps in the nightside ionosphere of Mars. *Earth, Planets and Space*,
753 *64*(2), 93–103. doi: 10.5047/eps.2011.04.010
- 754 Fillingim, M. O., Peticolas, L. M., Lillis, R. J., Brain, D. A., Halekas, J. S., Lum-
755 merzheim, D., & Bougher, S. W. (2010). Localized ionization patches in
756 the nighttime ionosphere of Mars and their electrodynamic consequences.
757 *Icarus*, *206*(1), 112–119. Retrieved from [http://dx.doi.org/10.1016/](http://dx.doi.org/10.1016/j.icarus.2009.03.005)
758 [j.icarus.2009.03.005](http://dx.doi.org/10.1016/j.icarus.2009.03.005) doi: 10.1016/j.icarus.2009.03.005
- 759 Forget, F., Hourdin, F., Fournier, R., Hourdin, C., Talagrand, O., Collins, M., ...
760 Huot, J. P. (1999). Improved general circulation models of the Martian at-

- 761 mosphere from the surface to above 80 km. *Journal of Geophysical Research:*
762 *Planets*, 104(E10), 24155–24175. doi: 10.1029/1999JE001025
- 763 Glassmeier, K. H., & Espley, J. (2013). ULF Waves in Planetary Magnetospheres.
764 *Magnetospheric ULF Waves: Synthesis and New Directions*, 169(d), 341–359.
765 doi: 10.1029/169GM22
- 766 González-Galindo, F., Chaufray, J.-Y., López-Valverde, M. A., Gilli, G., Forget,
767 F., Leblanc, F., ... Yagi, M. (2013). Three-dimensional Martian iono-
768 sphere model: I. The photochemical ionosphere below 180 km. *Journal*
769 *of Geophysical Research: Planets*, 118(10), 2105–2123. Retrieved from
770 <https://agupubs.onlinelibrary.wiley.com/doi/abs/10.1002/jgre.20150>
771 doi: 10.1002/jgre.20150
- 772 Gough, D. I., & Ingham, M. R. (1983). Interpretation methods for magnetometer
773 arrays. *Reviews of Geophysics*, 21(4), 805–827. Retrieved from [https://](https://agupubs.onlinelibrary.wiley.com/doi/abs/10.1029/RG021i004p00805)
774 agupubs.onlinelibrary.wiley.com/doi/abs/10.1029/RG021i004p00805
775 doi: <https://doi.org/10.1029/RG021i004p00805>
- 776 Grimm, R., Nguyen, T., Persyn, S., Phillips, M., Stillman, D., Taylor, T., ... Shep-
777 pard, D. (2021). A magnetotelluric instrument for probing the interiors of
778 Europa and other worlds. *Advances in Space Research*, 68(4), 2022–2037.
779 Retrieved from [https://www.sciencedirect.com/science/article/pii/](https://www.sciencedirect.com/science/article/pii/S0273117721002969)
780 [S0273117721002969](https://www.sciencedirect.com/science/article/pii/S0273117721002969) doi: <https://doi.org/10.1016/j.asr.2021.04.011>
- 781 Grimm, R. E., & Delory, G. T. (2012). Next-generation electromagnetic sounding
782 of the Moon. *Advances in Space Research*, 50(12), 1687–1701. Retrieved from
783 <http://dx.doi.org/10.1016/j.asr.2011.12.014> doi: 10.1016/j.asr.2011.12
784 .014
- 785 Halekas, J. S., Ruhunusiri, S., Harada, Y., Collinson, G., Mitchell, D. L., Mazelle,
786 C., ... Jakosky, B. M. (2017). Structure, dynamics, and seasonal variability
787 of the Mars-solar wind interaction: MAVEN Solar Wind Ion Analyzer in-flight
788 performance and science results. *Journal of Geophysical Research: Space*
789 *Physics*, 122(1), 547–578. doi: 10.1002/2016JA023167
- 790 Hall, J. L., Pauken, M. T., Kerzhanovich, V. V., Walsh, G. J., Fairbrother, D.,
791 Shreves, C., & Lachenmeier, T. (2007). Flight test results for aerially deployed
792 mars balloons. *AIAA Balloon Systems Conference, 2007*, 262–274.
- 793 Harada, Y., Ruhunusiri, S., Halekas, J. S., Espley, J., DiBraccio, G. A., Mcfadden,
794 J. P., ... Jakosky, B. M. (2019). Locally Generated ULF Waves in the Mar-
795 tian Magnetosphere: MAVEN Observations. *Journal of Geophysical Research:*
796 *Space Physics*, 124(11), 8707–8726. doi: 10.1029/2019JA027312
- 797 Hassler, D. M., Zeitlin, C., Wimmer-Schweingruber, R. F., Böttcher, S., Martin, C.,
798 Andrews, J., ... Cucinotta, F. A. (2012). The Radiation Assessment De-
799 tector (RAD) investigation. *Space Science Reviews*, 170(1-4), 503–558. doi:
800 10.1007/s11214-012-9913-1
- 801 Jakosky, B. M., Lin, R. P., Grebowsky, J. M., Luhmann, J. G., Mitchell, D. F.,
802 Beutelschies, G., ... Zurek, R. (2015). The Mars Atmosphere and
803 Volatile Evolution (MAVEN) Mission. *Space Science Reviews*, 3–48. Re-
804 trieved from <http://dx.doi.org/10.1007/s11214-015-0139-x> doi:
805 10.1007/s11214-015-0139-x
- 806 Johnson, C. L., Mittelholz, A., Langlais, B., Russell, C. T., Ansan, V., Banfield,
807 D., ... Banerdt, W. B. (2020). Crustal and time-varying magnetic fields
808 at the InSight landing site on Mars. *Nature Geoscience*, 13(3), 199–204.
809 Retrieved from <http://dx.doi.org/10.1038/s41561-020-0537-x> doi:
810 10.1038/s41561-020-0537-x
- 811 Joy, S. P., Mafi, J. N., & Slavney, S. (2019). Interior Exploration Using Seismic In-
812 vestigations, Geodesy, and Heat Transport (InSight) Mission Insight Fluxgate
813 Magnetometer (IFG) PDS Archive Software Interface Specification.
814 doi: <https://doi.org/10.17189/1519206>

- 815 Knapmeyer-Endrun, B., Panning, M. P., Bissig, F., Joshi, R., Khan, A., Kim, D., ...
816 Banerdt, W. B. (2021). Thickness and structure of the martian crust from In-
817 Sight seismic data. *Science*, *373*(6553), 438–443. doi: 10.1126/science.abf8966
- 818 Kurgansky, M. V., Baez, L., & Ovalle, E. M. (2007). A simple model of the mag-
819 netic emission from a dust devil. *Journal of Geophysical Research E: Planets*,
820 *112*(11), 1–7. doi: 10.1029/2007JE002952
- 821 Langlais, B., Thébaud, E., Houliez, A., Purucker, M. E., & Lillis, R. J. (2019).
822 A New Model of the Crustal Magnetic Field of Mars Using MGS and
823 MAVEN. *Journal of Geophysical Research: Planets*, *124*(6), 1542–1569. doi:
824 10.1029/2018JE005854
- 825 Lee, C. O., Hara, T., Halekas, J. S., Thiemann, E., Chamberlin, P., Eparvier, F.,
826 ... Jakosky, B. M. (2017). MAVEN observations of the solar cycle 24 space
827 weather conditions at Mars. *Journal of Geophysical Research: Space Physics*,
828 *122*(3), 2768–2794. doi: 10.1002/2016JA023495
- 829 Lee, C. O., Jakosky, B. M., Luhmann, J. G., Brain, D. A., Mays, M. L., Has-
830 sler, D. M., ... Halekas, J. S. (2018). Observations and Impacts of the
831 10 September 2017 Solar Events at Mars: An Overview and Synthesis of
832 the Initial Results. *Geophysical Research Letters*, *45*(17), 8871–8885. doi:
833 10.1029/2018GL079162
- 834 Lillis, R. J., Fillingim, M. O., Ma, Y., Gonzalez-Galindo, F., Forget, F., John-
835 son, C. L., ... Fowler, C. M. (2019). Modeling Wind-Driven Iono-
836 spheric Dynamo Currents at Mars: Expectations for InSight Magnetic Field
837 Measurements. *Geophysical Research Letters*, *46*(10), 5083–5091. doi:
838 10.1029/2019GL082536
- 839 Lillis, R. J., Robbins, S., Manga, M., Halekas, J. S., & Frey, H. V. (2013). Time
840 history of the Martian dynamo from crater magnetic field analysis. *Journal of*
841 *Geophysical Research E: Planets*, *118*(7), 1488–1511. doi: 10.1002/jgre.20105
- 842 Lorenz, R. D., Lemmon, M. T., & Maki, J. (2021). First Mars year of ob-
843 servations with the InSight solar arrays: Winds, dust devil shadows, and
844 dust accumulation. *Icarus*, *364*, 114468. Retrieved from [https://](https://www.sciencedirect.com/science/article/pii/S0019103521001494)
845 www.sciencedirect.com/science/article/pii/S0019103521001494 doi:
846 <https://doi.org/10.1016/j.icarus.2021.114468>
- 847 Luhmann, J. G., Dong, C. F., Ma, Y. J., Curry, S. M., Xu, S., Lee, C. O., ...
848 Jakosky, B. M. (2017). Martian magnetic storms. *Journal of Geophysical*
849 *Research: Space Physics*, *122*(6), 6185–6209. doi: 10.1002/2016JA023513
- 850 Luo, H., Du, A. M., Ge, Y. S., Johnson, C. L., Mittelholz, A., Zhang, Y., ... Xu,
851 W. Y. (2022). Natural Orthogonal Component Analysis of Daily Magnetic
852 Variations at the Martian Surface: InSight Observations. *Journal of Geophys-
853 ical Research: Planets*, *127*(2), 1–15. doi: 10.1029/2021JE007112
- 854 Mimoun, D., Murdoch, N., Lognonné, P., Hurst, K., Pike, W. T., Hurley, J., ...
855 Banerdt, W. B. (2017). The Noise Model of the SEIS Seismometer of
856 the InSight Mission to Mars. *Space Science Reviews*, *211*(1-4), 383–428.
857 Retrieved from <http://dx.doi.org/10.1007/s11214-017-0409-x> doi:
858 10.1007/s11214-017-0409-x
- 859 Mittelholz, A., & Johnson, C. L. (2022). The Martian Crustal Magnetic Field.
860 *Frontiers in Astronomy and Space Sciences*, *9*(895362). doi: 10.3389/
861 fspas.2022.895362
- 862 Mittelholz, A., Grayver, A., Khan, A., & Kuvshinov, A. (2021). The Global Con-
863 ductivity Structure of the Lunar Upper and Mid Mantle. *Journal of Geophys-
864 ical Research: Planets*, *126*(111), e2021JE006980. Retrieved from [https://](https://agupubs.onlinelibrary.wiley.com/doi/abs/10.1029/2021JE006980)
865 agupubs.onlinelibrary.wiley.com/doi/abs/10.1029/2021JE006980 doi:
866 <https://doi.org/10.1029/2021JE006980>
- 867 Mittelholz, A., Heagy, L., Johnson, C. L., Langlais, B., Lillis, R. J., & Rapin, W.
868 (2022). Helicopter Magnetic Field Surveys for Future Mars Missions. *LPI*
869 *Contributions*, *2655*, 5016.

- 870 Mittelholz, A., Johnson, C., Grimm, R., Haviland, H., Langlais, B., Lognonné, P.,
871 ... Banerdt, W. (2020, dec). Towards magnetic sounding of Mars using
872 diurnal variations. In *Agu fall meeting abstracts* (Vol. 2020, pp. DI026–03).
- 873 Mittelholz, A., Johnson, C. L., Feinberg, J. M., Langlais, B., & Phillips, R. J.
874 (2020). Timing of the martian dynamo : New constraints for a core field
875 4 . 5 and 3 . 7 Ga ago. *Science Advances*, 18(May), 1–8. doi: 10.1126/
876 sciadv.aba0513
- 877 Mittelholz, A., Johnson, C. L., Fillingim, M., Joy, S., Espley, J. R., Halekas, J., ...
878 Banerdt, W. (2021). Space Weather Observations with InSight. *Geophysical
879 Research Letters*.
- 880 Mittelholz, A., Johnson, C. L., & Lillis, R. J. (2017). Global-scale External Mag-
881 netic Fields at Mars Measured at Satellite Altitude. *Journal of Geophysical
882 Research: Planets*, 112, 1243–1257. Retrieved from [http://doi.wiley.com/
883 10.1002/2017JE005308](http://doi.wiley.com/10.1002/2017JE005308) doi: 10.1002/2017JE005308
- 884 Mittelholz, A., Johnson, C. L., & Morschhauser, A. (2018). A New Magnetic Field
885 Activity Proxy for Mars From MAVEN Data. *Geophysical Research Letters*,
886 45(12), 5899–5907. Retrieved from [https://agupubs.onlinelibrary.wiley
887 .com/doi/abs/10.1029/2018GL078425](https://agupubs.onlinelibrary.wiley.com/doi/abs/10.1029/2018GL078425) doi: 10.1029/2018GL078425
- 888 Mittelholz, A., Johnson, C. L., Thorne, S. N., Joy, S., Barrett, E., Fillingim, M. O.,
889 ... Banerdt, W. B. (2020). The Origin of Observed Magnetic Variability for a
890 Sol on Mars From InSight. *Journal of Geophysical Research: Planets*, 125(9),
891 1–14. doi: 10.1029/2020JE006505
- 892 Mittelholz, A., Johnson, C. L., Thorne, S. N., Yau, V., Joy, S., Barrett, E., ... Oth-
893 ers (2021). Magnetic Variations of a Sol Observed Over a Year on Mars with
894 InSight. In *Lunar and planetary science conference* (p. 1941).
- 895 Morgan, D. D., Gurnett, D. A., Kirchner, D. L., Fox, J. L., Nielsen, E., & Plaut,
896 J. J. (2008). Variation of the Martian ionospheric electron density from Mars
897 Express radar soundings. *Journal of Geophysical Research: Space Physics*,
898 113(9), 1–15. doi: 10.1029/2008JA013313
- 899 Nagy, A. F., Winterhalter, D., Sauer, K., Cravens, T. E., Brecht, S., Mazelle, C.,
900 ... Trotignon, J. G. (2004). The plasma Environment of Mars. *Space Sci-
901 ence Reviews*, 111(1), 33–114. Retrieved from [https://doi.org/10.1023/B:
902 SPAC.0000032718.47512.92](https://doi.org/10.1023/B:SPAC.0000032718.47512.92) doi: 10.1023/B:SPAC.0000032718.47512.92
- 903 Olsen, N. (1999). Induction studies with satellite data. *Surveys in Geophysics*, 20(3
904 - 4), 309–340. Retrieved from <http://dx.doi.org/10.1023/A:1006611303582>
905 doi: 10.1023/A:1006611303582
- 906 Olsen, N., Glassmeier, K. H., & Jia, X. (2010). Separation of the magnetic field into
907 external and internal parts. *Space Science Reviews*, 152(1-4), 135–157. doi: 10
908 .1007/s11214-009-9563-0
- 909 Perrin, C., Rodriguez, S., Jacob, A., Lucas, A., Spiga, A., Murdoch, N., ... Banerdt,
910 W. B. (2020). Monitoring of Dust Devil Tracks Around the InSight Land-
911 ing Site, Mars, and Comparison With In Situ Atmospheric Data. *Geophys-
912 ical Research Letters*, 47(10), e2020GL087234. Retrieved from [https://
913 agupubs.onlinelibrary.wiley.com/doi/abs/10.1029/2020GL087234](https://agupubs.onlinelibrary.wiley.com/doi/abs/10.1029/2020GL087234) doi:
914 <https://doi.org/10.1029/2020GL087234>
- 915 Pinçon, J.-L., Menvielle, M., & Szarka, L. (2000). Geomagnetic induction study
916 using the NetLander network of magnetometers. *Planetary and Space Sci-
917 ence*, 48(12), 1261–1270. Retrieved from [https://www.sciencedirect.com/
918 science/article/pii/S0032063300001082](https://www.sciencedirect.com/science/article/pii/S0032063300001082) doi: [https://doi.org/10.1016/
919 S0032-0633\(00\)00108-2](https://doi.org/10.1016/S0032-0633(00)00108-2)
- 920 Ramstad, R., Brain, D. A., Dong, Y., Espley, J., Halekas, J., & Jakosky, B. (2020).
921 The global current systems of the Martian induced magnetosphere. *Nature
922 Astronomy*. Retrieved from <https://doi.org/10.1038/s41550-020-1099-y>
923 doi: 10.1038/s41550-020-1099-y

- 924 Russell, C. T., & Joy, S. P. (2020). InSight IFG Magnetometer Mars Calibrated
 925 Data Collection. *NASA Planetary Data System*. doi: [https://doi.org/](https://doi.org/10.17189/1519202)
 926 [10.17189/1519202](https://doi.org/10.17189/1519202)
- 927 Sagdeev, R. Z., & Zakharov, A. V. (1989). Brief history of the Phobos mission. *Nature*, *341*, 581–585.
 928
- 929 Schubert, G., Russell, C. T., & Moore, W. B. (2000). Geophysics: Timing of the
 930 Martian dynamo. *Nature*, *408*(6813), 666–667. Retrieved from [http://www](http://www.nature.com/doi/10.1038/35047163)
 931 [.nature.com/doi/10.1038/35047163](http://www.nature.com/doi/10.1038/35047163) doi: 10.1038/35047163
- 932 Smrekar, S. E., Lognonné, P., Spohn, T., Banerdt, W. B., Breuer, D., Christensen,
 933 U., ... Wieczorek, M. (2018, dec). Pre-mission InSights on the Interior of
 934 Mars. *Space Science Reviews*, *215*(1), 3. Retrieved from [https://doi.org/](https://doi.org/10.1007/s11214-018-0563-9)
 935 [10.1007/s11214-018-0563-9](https://doi.org/10.1007/s11214-018-0563-9) doi: 10.1007/s11214-018-0563-9
- 936 Sonett, C. P. (1982). Electromagnetic induction in the Moon. *Reviews of Geo-*
 937 *physics*, *20*(3), 411–455. Retrieved from [https://agupubs.onlinelibrary](https://agupubs.onlinelibrary.wiley.com/doi/abs/10.1029/RG020i003p00411)
 938 [.wiley.com/doi/abs/10.1029/RG020i003p00411](https://agupubs.onlinelibrary.wiley.com/doi/abs/10.1029/RG020i003p00411) doi: [https://doi.org/](https://doi.org/10.1029/RG020i003p00411)
 939 [10.1029/RG020i003p00411](https://doi.org/10.1029/RG020i003p00411)
- 940 Spiga, A., Murdoch, N., Lorenz, R., Forget, F., Newman, C., Rodriguez, S., ...
 941 Banerdt, W. B. (2021). A Study of Daytime Convective Vortices and Tur-
 942 bulence in the Martian Planetary Boundary Layer Based on Half-a-Year of
 943 InSight Atmospheric Measurements and Large-Eddy Simulations. *Journal of*
 944 *Geophysical Research: Planets*, *126*(1), 1–28. doi: 10.1029/2020JE006511
- 945 Thomas, P., & Gierasch, P. J. (1985). Dust Devils on Mars. *Science*, *230*(4722),
 946 175–177. Retrieved from [https://science.sciencemag.org/content/230/](https://science.sciencemag.org/content/230/4722/175)
 947 [4722/175](https://science.sciencemag.org/content/230/4722/175) doi: 10.1126/science.230.4722.175
- 948 Thorne, S. N., Johnson, C. L., Mittelholz, A., Langlais, B., Lorenz, R., Murdoch,
 949 N., ... Banerdt, W. B. (2022). Investigation of magnetic field signals dur-
 950 ing vortex-induced pressure drops at InSight. *Planetary and Space Science*,
 951 105487. Retrieved from [https://www.sciencedirect.com/science/article/](https://www.sciencedirect.com/science/article/pii/S0032063322000733)
 952 [pii/S0032063322000733](https://www.sciencedirect.com/science/article/pii/S0032063322000733) doi: <https://doi.org/10.1016/j.pss.2022.105487>
- 953 Thorne, S. N., Mittelholz, A., Johnson, C. L., Joy, S., Liu, X., Russell, C. T., ...
 954 Banerdt, W. B. (2020). InSight fluxgate magnetometer data calibration
 955 assessment and implications. In *Lunar and planetary science conference*.
- 956 VanderPlas, J. T. (2017). Understanding the lomb-scargle periodogram. *arXiv*,
 957 *236*(1), 16. Retrieved from <http://dx.doi.org/10.3847/1538-4365/aab766>
 958 doi: 10.3847/1538-4365/aab766
- 959 Vervelidou, F., Lesur, V., Grott, M., Morschhauser, A., & Lillis, R. J. (2017). Con-
 960 straining the Date of the Martian Dynamo Shutdown by Means of Crater
 961 Magnetization Signatures. *Journal of Geophysical Research: Planets*, *122*(11),
 962 2294–2311. doi: 10.1002/2017JE005410
- 963 Vozoff, K. (1991). THE MAGNETOTELLURIC METHOD. In *Electromagnetic*
 964 *methods in applied geophysics: Volume 2, application, parts a and b*. Society
 965 of Exploration Geophysicists. Retrieved from [https://doi.org/10.1190/](https://doi.org/10.1190/1.9781560802686.ch8)
 966 [1.9781560802686.ch8](https://doi.org/10.1190/1.9781560802686.ch8) doi: 10.1190/1.9781560802686.ch8
- 967 Wieczorek, M. A., Broquet, A., McLennan, S. M., Rivoldini, A., Golombek,
 968 M., Antonangeli, D., ... Banerdt, W. B. (2022). InSight constraints
 969 on the global character of the Martian crust. *Journal of Geophysical Re-*
 970 *search: Planets*, *n/a*(n/a), e2022JE007298. Retrieved from [https://](https://agupubs.onlinelibrary.wiley.com/doi/abs/10.1029/2022JE007298)
 971 agupubs.onlinelibrary.wiley.com/doi/abs/10.1029/2022JE007298 doi:
 972 <https://doi.org/10.1029/2022JE007298>
- 973 Withers, P. (2009). A review of observed variability in the dayside ionosphere of
 974 Mars. *Advances in Space Research*, *44*(3), 277–307. Retrieved from [http://dx](http://dx.doi.org/10.1016/j.asr.2009.04.027)
 975 [.doi.org/10.1016/j.asr.2009.04.027](http://dx.doi.org/10.1016/j.asr.2009.04.027) doi: 10.1016/j.asr.2009.04.027
- 976 Withers, P., & Pratt, R. (2013). An observational study of the response of the upper
 977 atmosphere of Mars to lower atmospheric dust storms. *Icarus*, *225*(1), 378–
 978 389. Retrieved from <https://www.sciencedirect.com/science/article/>

979 pii/S0019103513001267 doi: <https://doi.org/10.1016/j.icarus.2013.02.032>
980 Xu, S., Curry, S. M., Mitchell, D. L., Luhmann, J. G., Lillis, R. J., & Dong, C.
981 (2019). Magnetic Topology Response to the 2003 Halloween ICME Event at
982 Mars. *Journal of Geophysical Research: Space Physics*, *124*(1), 151–165. doi:
983 10.1029/2018JA026118